JGR Earth Surface

RESEARCH ARTICLE
10.1029/2024JF007689

Dynamic Simulation of Rock-Avalanche Fragmentation

Shiva P. Pudasaini[1,2], Martin Mergili[3], Qiwen Lin[4], and Yufeng Wang[4]

[1]School of Engineering and Design, Civil and Environmental Engineering, Technical University of Munich, Munich, Germany, [2]Kathmandu Institute of Complex Flows, Kageshwori Manohara Municipality, Bhadrabas, Kathmandu, Nepal, [3]Department of Geography and Regional Science, University of Graz, Graz, Austria, [4]Faculty of Geosciences and Environmental Engineering, Department of Geological Engineering, Southwest Jiaotong University, Chengdu, China

Key Points:

- We propose a novel, unified dynamic simulation method for rock-avalanche fragmentation and propagation
- It includes mechanically controlled rock deformation, momentum loss at impact and energy transfer in fragmentation generating lateral pressure
- Dynamic fragmentation resulting from overcoming of tensile strength leads to enhanced spreading, thinning, and hypermobility of rock-avalanches

Supporting Information:

Supporting Information may be found in the online version of this article.

Correspondence to:

S. P. Pudasaini,
shiva.pudasaini@tum.de

Citation:

Pudasaini, S. P., Mergili, M., Lin, Q., & Wang, Y. (2024). Dynamic simulation of rock-avalanche fragmentation. *Journal of Geophysical Research: Earth Surface*, *129*, e2024JF007689. https://doi.org/10.1029/2024JF007689

Received 14 FEB 2024
Accepted 4 AUG 2024

Author Contributions:

Conceptualization: Shiva P. Pudasaini
Data curation: Shiva P. Pudasaini, Martin Mergili
Formal analysis: Shiva P. Pudasaini, Martin Mergili
Funding acquisition: Shiva P. Pudasaini, Martin Mergili, Qiwen Lin, Yufeng Wang
Investigation: Qiwen Lin, Yufeng Wang
Methodology: Shiva P. Pudasaini, Martin Mergili
Project administration: Shiva P. Pudasaini, Martin Mergili, Qiwen Lin, Yufeng Wang
Resources: Shiva P. Pudasaini, Martin Mergili
Software: Shiva P. Pudasaini, Martin Mergili

Abstract Fragmentation is a common phenomenon in complex rock-avalanches. The fragmentation intensity and process determines exceptional spreading of such mass movements. However, studies focusing on the simulation of fragmentation are still limited and no operational dynamic simulation model of fragmentation has been proposed yet. By enhancing the mechanically controlled landslide deformation model (Pudasaini & Mergili, 2024, https://doi.org/10.1029/2023jf007466), we propose a novel, unified dynamic simulation method for rock-avalanche fragmentation. The model includes three important aspects: mechanically controlled rock mass deformation, momentum loss while the rock mass fiercely impacts the ground, and the energy transfer during fragmentation resulting in the generation of dispersive lateral pressure. We reveal that the dynamic fragmentation, resulting from the overcoming of the tensile strength by the impact on the ground, leads to enhanced spreading, thinning, run-out and hypermobility of rock-avalanches. Thereby, the elastic strain energy release caused by fragmentation becomes an important process. Energy conversion between the front and rear parts caused by the fragmentation results in the enhanced forward movement of the front and hindered motion of the rear of the rock-avalanche. The new model describes this by amplifying the lateral pressure gradient in the opposite direction: enhanced for the frontal particles and reduced for the rear particles after the fragmentation. The main principle is the switching between the compressional stress and the tensile stress, and therefore from the controlled deformation to substantial spreading of the frontal part in the flow direction while backward stretching of the rear part of the rock mass. Laboratory experiments and field events support our simulation results.

Plain Language Summary Rock-avalanches often fragment into pieces when they slide down mountain slopes. Fragmentation converts the rock mass into a deformable granular avalanche. This leads to high-velocity fragments, resulting in more extensive lateral spreading of rock particles. However, no operational dynamic simulation model exists to describe rock fragmentation and the subsequent granular avalanche. Here, we introduce a simple model for the simulation of rock-avalanche fragmentation dynamics that unifies important processes of mechanically controlled deformation, momentum loss as the rock mass impacts the ground, fragmentation, energy conversion among fragmented clasts and the induced dispersive pressure. The model is capable of automatically simulating rock mass movements as rigid blocks, the fragmentation of these blocks into granular avalanches, and the deposition process. This explains many important phenomena observed in fragmenting rock-avalanches, including the exceptional lateral spreading, thinning, and hypermobility in the run-out zone. We implement this model in the freely available computer simulation program r.avaflow, and present some tests on simple computer-generated landscapes to demonstrate that the model works well.

1. Introduction

Large rock slides or rock falls usually fragment into pieces when they impact the ground, experience a sudden decrease of the slope angle in the direction of the flow path, or hit a rock wall or a counter-slope. This converts the previously solid-like sliding rock mass into a largely deformable granular avalanche of fragmented rock particles (T. R. Davies & McSaveney, 2002; Stead et al., 2006; Eberhardt et al., 2004; Gao et al., 2021; S.-L. Zhang et al., 2023). Figure 1 shows some examples of rock-avalanches with fragmentation. Observations suggest that deposits of large rock-avalanches consist predominantly of fragmented rock debris with exceptionally long run-out (T. R. Davies & McSaveney, 2009; Dufresne et al., 2016; Q. Lin et al., 2022). Rock fragmentation results in high-velocity fragments of the moving rock mass leading to more extensive longitudinal spreading of the rock particles, compared to non-fragmenting granular avalanches (Haug et al., 2021). Consequently, the increased

Supervision: Shiva P. Pudasaini
Validation: Shiva P. Pudasaini, Martin Mergili, Qiwen Lin, Yufeng Wang
Visualization: Shiva P. Pudasaini, Martin Mergili
Writing – original draft: Shiva P. Pudasaini, Martin Mergili
Writing – review & editing: Shiva P. Pudasaini, Martin Mergili, Qiwen Lin, Yufeng Wang

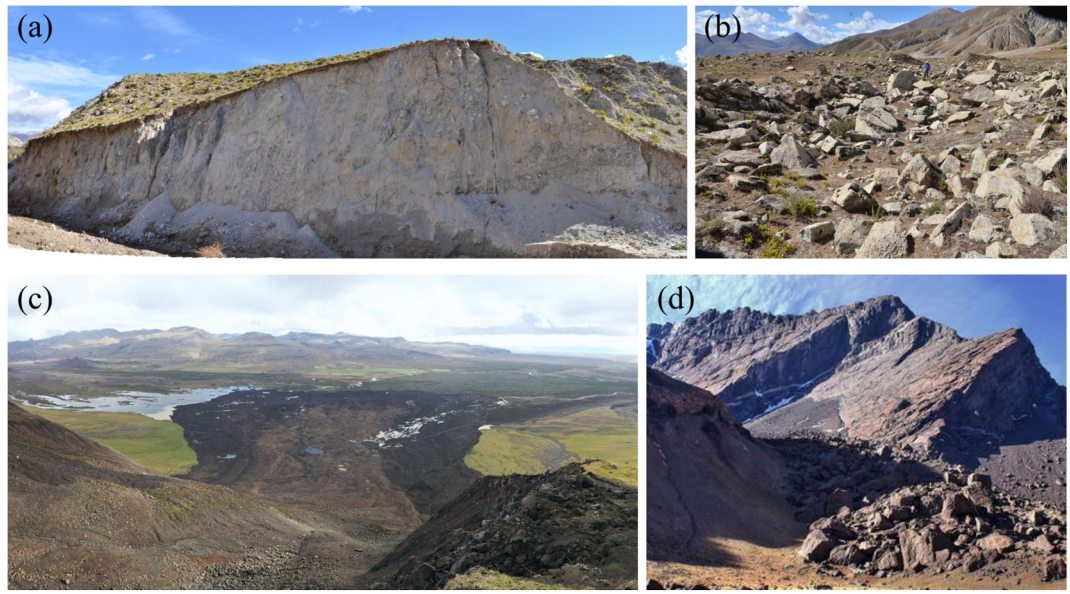

Figure 1. Examples of rock avalanches with fragmented deposit that is substantially finer than the bedrock in the source area. (a) Differential fragmentation in the outcrop, and (b) the fragmented blocks on the surface of the deposit of the giant prehistoric Nyixoi Chongco rock avalanche in Tibet, China (Wang et al., 2018). (c) The Hitardalur rock-avalanche, Iceland, of 7 July 2018 composed of exceptionally fragmented clasts, characterized by a very high mobility. (d) Prehistoric Cerro Tolosa rock avalanche, Argentine Andes with fragmented clasts deposited at the toe of the slope.

mobility and run-out of the rock avalanche is proposed to be the result of this additional fragmentation-induced spreading (T. R. Davies & McSaveney, 2009).

At the very beginning of its impact at the ground, the velocity of the entire moving mass can be the same as if it was a rigid body. However, as the coherent block-type rock mass impacts the ground, and as fragmentation occurs, the velocities of the front and the rear masses become substantially different. The impact converts the remaining strain energy (the elastic and inelastic strain energy) stored in the fragmented rock mass into the kinetic energy of the fragments. This may energize the fragments even to fly outward during dynamic fragmentation, as observed in laboratory experiments (Bowman et al., 2012; Q.-W. Lin et al., 2020). At the local fragmentation stage, there is an increasing trend of velocity and kinetic energy at the front part of the rock mass, and an opposite trend at the rear part, as experiments have shown (Q. Lin et al., 2022).

Aiming to explain the frequent occurrence of fragmentation in rock-avalanches, a fragmentation spreading model was proposed by T. R. Davies et al. (1999), who argued that the extraordinarily long run-out of rock-avalanches would result from the continuous fragmentation of the clasts through the different stages of the motion. They propose that the strong dispersive pressure (pressure generated by stress fluctuation or fragmentation: Bagnold (1954), Melosh (1986), T. R. Davies et al. (1999)) originates from the elastic energy transfer, enhancing the kinetic energy of the fragmented rock particles during the process of fragmentation. Laboratory experiments and simulation results show that the velocity of frontal masses strongly increase after impact-fragmentation but in the run-out, the center of mass is usually pushed back indicating a high energy consumption (Bowman et al., 2012; Q. Lin et al., 2022; S.-L. Zhang et al., 2023). However, how fragmentation and dispersive pressure are related is still a subject of discussion and yet to be recorded in natural cases. Additionally, fracturing and fragmentation inevitably consume part of the elastic energy, which leads to different arguments about dispersive pressure-induced hypermobility caused by fragmentation (T. R. H. Davies et al., 2020; Locat et al., 2006). In recent years, fluctuated stress (the component of the total stress other than the overburden load) has been monitored in experiments and reproduced in simulations. This type of stress is regarded as one reason for the high mobility of rock-avalanches and might possibly explain the dispersive stress (Choi & Goodwin, 2021; K. Li et al., 2022; Lima, 2010; Taberlet et al., 2007). Yet, the flow mobility can be enhanced by different mechanisms. An extensive list of transport mechanisms has been proposed to explain reduced friction and the hypermobility of large avalanches. This includes: large volume, fine powders at the base, interstitial fluids, pore fluid pressure, air pockets,

dispersive grain flow, local steam generation, frictionites, lubrication, fluidization, entrainment of the bed material, oscillation, and dynamic fragmentation (Cagnoli, 2024; Cagnoli & Quareni, 2009; Collins & Melosh, 2003; T. R. H. Davies, 1982; T. R. Davies & McSaveney, 2009; T. R. Davies et al., 1999; T. Davies et al., 2010; Hsu, 1975; Kent, 1966; Legros, 2002; Pudasaini & Krautblatter, 2021; Pudasaini & Miller, 2013; Shreve, 1966).

Some simulations have also been conducted to reproduce the fragmentation-induced run-out of rock avalanches (T. R. Davies & McSaveney, 2002; Eberhardt et al., 2004; Gao et al., 2021; Stead et al., 2006). However, the fragmentation of rock-avalanches involves the initiation and propagation of fractures, which is a highly non-linear process requiring complex models even for the simplest configuration (Turcotte, 1997). No general and unified dynamic simulation model exists to date to describe rock-fragmentation resulting in avalanching rock particles, induced additional spreading and run-out of rock avalanches. Therefore, based on a continuum mechanical framework, we propose the first such formally derived dynamic model and simulation technique for dynamic fragmentation and the associated granular rock mass propagation, spreading, and deposition. We expect to provide insights into the effects of fragmentation on rock avalanche dynamics. Here, we focus on presenting the model and its sensitivity analysis with the involved physical parameters and the mechanical aspects. Application of the proposed model against real events from the field is out of scope here, and should be dealt with separately.

The proposed model includes the mechanically controlled deformation before the fragmentation, momentum loss during the avalanche impact at the ground, fragmentation and overcoming of the mechanical control against the deformation potential, conversion of the elastic strain energy into the kinetic energy of the fragmented clasts, mainly caused by the impact with the ground, but also due to particle interactions during motion, and the induced dispersive pressure that is combined with the lateral hydraulic pressure gradient. Depending on the particular event, the fragmentation mechanism can be employed through the whole track, or for a given sector. The new model explains many important phenomena observed in fragmenting rock avalanches, including the exceptional lateral spreading, thinning, and hypermobility in the run-out zone.

2. A Unified Dynamic Avalanche Fragmentation Model

2.1. The Fragmentation Mechanism

The dynamic fragmentation of an intact block is violent and rapid. Generally, the disintegration of rock masses along joints may occur during the initial stage of the movement. However, the fragmentation may also take place after a while as the block-type sliding mass impacts the ground, or the shear force acts continuously before the rock avalanche stops (Perinotto et al., 2015; M. Zhang & McSaveney, 2017; M. Zhang et al., 2019). Both the fragmentation along joints and of intact blocks play an important role in determining the run-out behavior of a rock avalanche. During the fragmentation of the rock mass, the fracturing process along some preexisting joints and newly generated joints overcomes their tensile strengths. In this process, the velocity of the system changes. As it does, the slope parallel velocity (and therefore also the kinetic energy) of the frontal mass increases strongly. However, the velocity of the rear part of the mass decreases substantially. This describes the phenomenon of fragmentation-induced energy transfer (Q. Lin et al., 2020, 2022). The energy convey between the front and rear parts of the mass caused by the fragmentation process results in the enhanced forward movement of the front and the hindered movement of the rear portion of the rock-avalanche. And, it is argued that the fragmentation-induced energy transfer from the rear part to the frontal part is due to the release of elastic strain energy and its conversion to kinetic energy (Bowman et al., 2012; T. R. Davies & McSaveney, 2009; De Blasio & Crosta, 2015; X. B. Li et al., 2005; Z. X. Zhang et al., 2000). However, at least two questions remain unsolved: (a) Which factors influence the energy transfer and hyperspreading in the deposition area; and (b) what are the internal mechanisms involved in this phenomenon? To answer these questions, we propose a unified theoretical model and simulation technique. It is revealed that this process is tightly coupled with the prevailing mechanically controlled deformation, momentum loss due to the impact, and the lateral pressure of the rock mass.

The elastic strain energy release caused by fragmentation is an important dynamic process (X. B. Li et al., 2005; Z. X. Zhang et al., 2000). As the rock mass slides down and experiences a sharp decrease of the slope, part of its kinetic energy is transformed into elastic strain energy stored in bonds. Then, already during the mass collapse, due to shearing, or once the impact force is larger than the bond strength near the transition zone, the bond breaks. Importantly, in the meantime, the elastic strain energy stored in the entire rock mass is released. Eventually, this process converts the strain energy into the kinetic energy of fragments, enhancing the kinetic energy of the rock mass (Q.-W. Lin et al., 2020; Q. Lin et al., 2022).

There are three important phenomena tightly connected to fragmentation. First, as the rock mass impacts the ground, or experiences a sharp decrease in slope, part of its momentum is lost. We dynamically consider this aspect by momentarily embedding (introducing) the momentum loss in the momentum balance equation. Second, as the longitudinal dispersive force acts effectively in the direction of decreasing mass depth, it causes the rear part of the avalanche to decelerate and halt and the front part to accelerate (T. R. Davies & McSaveney, 2009). Accompanied with the impact and fragmentation, a significant amount of the fragmented mass moves relatively slowly, mainly in the back, as compared to the non-fragmented solid-type mass, and substantially more slowly, compared to the frontal fragmented particles. Therefore, fragmentation results in the delayed movement of the center of the moving mass in comparison to the motion of a non-fragmented rigid-type mass. Third, the strong lateral (particularly longitudinal) dispersive pressure leads to exceptional spreading and long run-out of the fragmented mass. We mechanically model the second and third processes by including the longitudinal dispersive pressure in the momentum balance equation. This is done by dynamically enhancing the force induced by the lateral hydraulic pressure gradient induced by the free-surface of the landslide, the natural candidate to accommodate the lateral pressure. We dynamically combine the dispersive pressure with the lateral pressure gradient. In contrast to the mechanical control against deformation (Pudasaini & Mergili, 2024) that may prevent deformation of the rock mass for quite a while, this enhancement of the lateral pressure results in the frontal spreading, thinning of the rock mass, and a tremendous increase in the mobility of the avalanche.

2.2. Controlled Deformation, Momentum Loss, and Energy Transfer

There are three major components of the proposed fragmentation dynamics leading to the extraordinary avalanching motion.

2.2.1. Mechanically Controlled Rock Mass Deformation

After its release, the rock mass may freely deform as if it was a frictional granular material, or it may just slide as a rigid body virtually without any deformation. In general, based on its material strength against deformation, it may move with the mechanically controlled deformation mechanism applied in controlling the deformation potential induced by the force associated with the hydraulic pressure gradient. Here, we consider the mechanically controlled landslide deformation model proposed by Pudasaini and Mergili (2024):

$$\frac{\partial (hu)}{\partial t} + \frac{\partial}{\partial x}\left[hu^2 + K_x g^z \frac{h^2}{2}\left(1 - \frac{S_{M_p}}{\rho g^z}\right)\right] = h\left[\left\{g^x - \frac{u}{|u|}\mu_\delta\left(g^z + \kappa u^2\right)\right\} - C_{v_x} u|u|\right]. \tag{1}$$

In Equation 1, t [s] is time, x [m] is the distance along the slope, h [m] is the landslide depth in the direction perpendicular to the slope, and u [ms^{-1}] is the velocity along the x-direction. Similarly, g^x and g^z are the components of gravitational acceleration along and perpendicular (the z [m]-direction) to the slope, μ_δ [−] is the Coulomb friction coefficient, κ [m^{-1}] is the curvature of the slope, C_{v_x} [m^{-1}] is the viscous drag coefficient, K_x [−] is the earth pressure coefficient, and S_{M_p} [kg m^{-2}s^{-2}] (the specific weight of the avalanching mass) is the mechanical strength against deformation. The later controls the deformation induced by the force associated with the hydraulic pressure gradient (Pudasaini & Mergili, 2024) such that $S_{M_p}/(\rho g^z) \in (0,1)$. When $S_{M_p}/(\rho g^z) = 0$ the mass deforms as if it was a granular fluid (flow) as ruled by the lateral hydraulic pressure gradient. In contrast, when $S_{M_p}/(\rho g^z) = 1$ it slides virtually without any deformation, as a rigid body, because the tendency of the lateral hydraulic pressure gradient to cause deformation is fully controlled. So, any deformation scenarios can be described by adequate values of the mechanical strength S_{M_p} against deformation.

As can be seen from Equation 1, we can describe both the block sliding (elastic rigid material) without deformation when $S_{M_p}/(\rho g^z) = 1$, and the granular flow (granular plastic material) with deformation when $S_{M_p}/(\rho g^z) = 0$. Any other scenario in between can be described by considering the deformation controller $S_{M_p}/(\rho g^z)$ between 1 and 0. As we will show later, this plays a crucial role in the impact at the ground, fragmentation, and the subsequent granular flow dynamics and deposition.

2.2.2. Momentum Loss During Impact

As the block-type solid mass impacts the ground that can be on the inclined or the horizontal section of the surface, some of its momentum is lost. This is a complex process. However, the intensity and magnitude of the momentum loss depends on many factors, including the slope geometry and the material strength of the avalanche, mainly its physical properties, say M_l [s^{-1}], the momentum loss rate. The momentum is the product of the rock-avalanche mass and its velocity. It is therefore proportional to hu, and the momentum loss can be explained by $-M_l\, hu$. With this, we enhance the momentum balance Equation 1 by supplementing the source (right hand side) by the quantity $-M_l\, hu = -h[M_l\, u]$:

$$\frac{\partial(hu)}{\partial t} + \frac{\partial}{\partial x}\left[hu^2 + K_x g^z \frac{h^2}{2}\left(1 - \frac{S_{M_p}}{\rho g^z}\right)\right] = h\left[\left\{g^x - \frac{u}{|u|}\mu_\delta\left(g^z + \kappa u^2\right)\right\} - M_l u - C_{v_x} u|u|\right]. \tag{2}$$

By definition, $M_l \in (0, 1)$ models the momentum loss of the rock mass as it impacts the ground, and is a local quantity. In particular, $M_l \to 0$ indicates virtually no momentum loss akin to granular flows in smoothly varying slopes, whereas $M_l \to 1$ represents almost all momentum loss at impact, a scenario closer to the vertical fall of the rock mass.

2.2.3. The Energy Transfer During Fragmentation, and the Dispersive Lateral Pressure

As discussed earlier, the energy transfer during the fragmentation results in the dispersive lateral pressure. The rock-avalanche switches from controlled motion to fragmentation and then to granular flow. So, the effective lateral stress $K_x p_{zz} - K_x S_{M_p} h/2$ in Pudasaini and Mergili (2024) needs to be enhanced by a positive quantity $K_x S_{M_l} h/2$ that describes the dispersive pressure. Here, K_x is the earth pressure coefficient, S_{M_l} [kg $m^{-2}s^{-2}$] (has the dimension of the specific weight of the avalanching mass) is the dispersive pressure parameter describing the fragmentation induced enhanced lateral pressure, and $h/2$ emerges due to the consideration of the mean of the lateral pressure (Pudasaini & Mergili, 2024). Therefore, the total effective lateral pressure p_{xx} [m^2s^{-2}] (per unit density) for the fragmented rock now reads as:

$$p_{xx} = K_x p_{zz} - K_x S_{M_p} \frac{h}{2} + K_x S_{M_l} \frac{h}{2}, \tag{3}$$

where p_{zz} [m^2s^{-2}] is the overburden pressure (normalized with density) of the rock mass in the direction perpendicular to the slope. This combines the dispersive pressure $K_x S_{M_l} h/2$ with the compressional pressure $-K_x S_{M_p} h/2$ (Pudasaini & Mergili, 2024) against the usual lateral hydraulic pressure $K_x p_{zz}$ induced by the free-surface gradient of the rock mass (Pudasaini & Hutter, 2007). Moreover, as in the deformation controller $-K_x S_{M_p} h/2$ (Pudasaini & Mergili, 2024), K_x also appears in $K_x S_{M_l} h/2$ for the structural convenience. Otherwise, we could just use $S_{M_l} h/2$. This establishes a direct connection between the dispersive pressure and the lateral pressure gradient. It will become clearer in Section 2.3 where the unified momentum balance equation for fragmented rock-avalanches is presented.

In our modeling, the lateral earth pressure coefficient is dynamically determined by the mechanical functional relationship (Pudasaini & Hutter, 2007):

$$K_x = 2\sec^2\phi\left\{1 \mp \left(1 - \cos^2\phi \sec^2\delta\right)^{1/2}\right\} - 1, \tag{4}$$

where the $-$ sign indicates the active earth pressure coefficient $\left(K_x^a\right)$ when $\partial u/\partial x \geq 0$, describing an extensional motion, and the $+$ sign indicates the passive earth pressure coefficient $\left(K_x^p\right)$ when $\partial u/\partial x < 0$, describing a compactional motion. In Equation 4, ϕ [°] is the internal friction angle (friction between the granular particles in the avalanche), and δ [°] is the basal friction angle (friction between the avalanche and the sliding surface).

The dispersive pressure parameter S_{M_l} can be a complex quantity. It can be a constant, or a linear- or a non-linear function of several physical and dynamical quantities. As the fragmentation induces the dispersive pressure, this then requires the consistent enhancement of the term associated with the hydraulic pressure in the momentum

balance equation. Before the fragmentation process, S_{M_p} may be effective, while the lateral pressure parameter S_{M_l} may be ineffective. As the process of dynamic fragmentation begins, it activates S_{M_l} whereas S_{M_p} is (fully, or partly) de-activated. This is the main mechanical process and transition from solid-type motion to fragmentation to the avalanching motion of granular particles. Based on the intensity and mechanism of the disintegration and/or the impact on the ground and fragmentation, the dispersive lateral pressure S_{M_l} can even be much higher than the compressional pressure, S_{M_p}. This ultimately defines the thickness, spreading and mobility of the fragmented mass in the run-out zone. However, which parameter (S_{M_p} and/or S_{M_l}) is effective, when and how, and to which degree, is a technical question. It depends on the topographic situation, the material properties and the mechanical strength of the rock-avalanche, the disintegration process, the impact intensity and the fragmentation process. Consequently, these parameters should be properly defined and chosen by the practitioner. The possible range of physical parameters and mechanical constructs and their plausible estimates are provided later in Sections 3 and 4. However, it is out of scope here to provide guiding parameter values for practitioners. This will require calibration and evaluation with some well-documented real-world events. Here, we have provided a general frame for simulating rock-avalanche motion and spreading following its impact at the ground, disintegration and fragmentation.

Now, assuming the standard hydrostatic pressure distribution through the depth, $p_{zz} = (s - z)g^z$ (s [m] is the free-surface of the sliding mass), applying the gradient operator ($\partial/\partial x$) and depth averaging Equation 3 following the usual procedure (Pudasaini & Hutter, 2007; Pudasaini & Mergili, 2024), we obtain:

$$\frac{\partial}{\partial x}\left[K_x g^z \frac{h^2}{2}\left(1 - \frac{S_{M_p}}{\rho g^z} + \frac{S_{M_l}}{\rho g^z}\right)\right]. \tag{5}$$

This is the total effective lateral pressure gradient that systematically emerges in the proposed momentum balance equation below.

2.3. The Dynamic Rock-Avalanche Fragmentation Model: Geometrically Two-Dimensional

Although structurally simple, the three processes mentioned above, the mechanically controlled landslide deformation, the momentum loss in impact and the energy transfer resulting in the dispersive pressure, are mechanically complicated. We unify and formally include all these aspects in the momentum balance equation for the first time aiming at dynamically simulating the processes of controlled deformation, energy loss during impact, disintegration or fragmentation, energy transfer and the subsequent granular flow, exceptional spreading and hypermobility of the granular mass with unprecedented thinning in the run-out. With the three mechanical components mentioned above for the fragmented avalanche motion, generalizing Equation 2 with Equation 5, we obtain the unified mass and momentum balance equations:

$$\frac{\partial h}{\partial t} + \frac{\partial (hu)}{\partial x} = 0, \tag{6}$$

$$\frac{\partial (hu)}{\partial t} + \frac{\partial}{\partial x}\left[hu^2 + K_x g^z \frac{h^2}{2}\left(1 - \frac{S_{M_p}}{\rho g^z} + \frac{S_{M_l}}{\rho g^z}\right)\right] = h\left[\left\{g^x - \frac{u}{|u|}\mu_\delta\left(g^z + \kappa u^2\right)\right\} - M_l u - C_{v_x} u|u|\right]. \tag{7}$$

Equations 6 and 7 are written in conservative form. We call Equations 6 and 7 the dynamic simulation model for the rock-avalanche fragmentation. We call

$$S_{M_u} = -\left(\frac{S_{M_p}}{\rho g^z} - \frac{S_{M_l}}{\rho g^z}\right), \tag{8}$$

the unified mechanical strength that combines both the mechanical control against deformation and fragmentation-induced lateral pressure. It is a non-dimensional number. As the simulation results show later, S_{M_u} and M_l are central in the description of the fragmentation-induced rock-avalanche dynamics.

In laboratory experiments, the rock mass may be solid-like before impact, and it may become deformable and gain the dispersive lateral pressure after impact. Thus, impact-fragmentation may control both S_{M_p} and S_{M_l}. In this

situation, one may just use S_{M_l} to represent the combined effect caused by impact-fragmentation dynamics. For real-world rock-avalanches, due to the possible disintegration occurring at the very beginning, avalanche mass may always be deformable. Thus, it is often necessary that S_{M_l} is always activated, to some degree, high or low, depending on the situation. However, the fragmentation activity in the real-world event can be a progressive phenomenon during the entire motion of the rock-avalanche. So, depending on the process, S_{M_l} can be a variable (or a function) connected with the fragmentation process. Similarly, S_{M_p} may also vary with the avalanching process. In that situation, both S_{M_p} and S_{M_l} should be appropriately used in the simulation. However, the dynamics of S_{M_p} and S_{M_l} should be explored with the data from laboratory experiments and real-world events of rock-avalanches with fragmentation. Data may include the rock strength before fragmentation, strength loss during fragmentation, particle size, internal and basal friction, and speed during and after fragmentation.

As shown in Equation 7, eight different forces (or processes) are involved in the complexity of rock-avalanche fragmentation. These are the forces due to gravitational acceleration, friction, curvature, viscous drag, the hydraulic pressure gradient, mechanical control against deformation, momentum loss at impact and the dispersive pressure. We note that the viscous drag force is the force that is proportional to the square of the velocity of the moving rock mass (material or object), and is induced by the viscosity of the ambient fluid (air for subaerial rock-avalanches) (Pudasaini & Hutter, 2007; Pudasaini & Krautblatter, 2021). The gravitational acceleration, friction, curvature and the viscous drag lead to changes in the free surface gradient of the landslide. The deformation control mechanism involves the resistance against the deformation associated with the hydraulic pressure gradient, gravitational acceleration, friction, curvature and the viscous drag forces. The momentum loss updates the actual available energy after impact. And, the dispersive pressure enhances the lateral pressure gradient, causing the wide spreading in the run-out zone.

2.4. Advancement and the Model Structure

An important aspect of our model Equations 6 and 7 is that, by setting $M_l = 0$, $S_{M_p} = 0$ and $S_{M_l} = 0$, and imposing the linear increase of the earth pressure coefficients in its active and passive states by the same amount, but globally through the entire path of the propagating mass, we recover the model by T. R. Davies and McSaveney (2002). So, in this respect, our model may be perceived as an extension to the T. R. Davies and McSaveney (2002) model. However, here, we have fundamentally advanced by presenting a general, unified and flexible model for the fragmentation-induced rock-avalanche motion in a mechanically controlled manner. This was done by including the four important mechanical aspects associated with M_l, S_{M_p} and S_{M_l}, and by considering an automatically, dynamically evolving earth-pressure coefficient without any bias. Moreover, in our modeling frame, M_l, S_{M_p} and S_{M_l} can be constrained as local quantities.

As $S_{M_l} \to 0$ and $M_l \to 0$, Equations 6 and 7 reduce to the mechanically controlled landslide deformation model by Pudasaini and Mergili (2024). Thus, the advantage of the proposed model is that the existing efficient numerical methods (Pudasaini & Hutter, 2007) and computational tools, such as r.avaflow (Mergili & Pudasaini, 2024; Mergili et al., 2017) can be directly applied to the model Equations 6 and 7.

2.5. Essence of the Model

The novel unified dynamic fragmentation model Equations 6 and 7 developed here enhances the mechanically controlled deformation (with compressional strength) model proposed by Pudasaini and Mergili (2024) by embedding the two additional important aspects of momentum loss at impact and the mechanism of overcoming the tensile strength of the rock mass into the momentum balance equation. The unified mechanical strength for the controlled deformation plays the key role as dynamically ruled by the force associated with the hydraulic pressure gradient that precisely reigns the landslide deformation and spreading. Subsequent to the controlled deformation, the disintegration, impact and fragmentation processes, the new model describes the energy loss due to the impact and the energy conversion in fragmenting rock-avalanches by amplifying the hydraulic pressure gradient in the opposite direction: enhanced for the frontal particles and reduced for the rear particles. The main principle is the switching between the compressional stress (the controlled deformation) and the tensile stress and its overcoming due to fragmentation, resulting in the development of the dispersive pressure. This leads to the substantial spreading of the frontal part of the mass in the flow direction and, at the same time, the backward stretching of the

rear part of the rock mass. This also implies that fragmentation enhances the run-out, with less energy consumption compared to granular flows. We elaborate on this at Section 3.2.3.

2.6. The Dynamic Rock-Avalanche Fragmentation Model: Geometrically Three-Dimensional

Equations 6 and 7 can be directly extended to the evolution of geometrically three-dimensional landslide fragmentation and its dynamics as:

$$\frac{\partial h}{\partial t}+\frac{\partial (hu)}{\partial x}+\frac{\partial (hv)}{\partial y}=0, \tag{9}$$

$$\frac{\partial (hu)}{\partial t}+\frac{\partial}{\partial x}\left[hu^2+K_x g^z\frac{h^2}{2}\left(1-\frac{S_{M_p}}{\rho g^z}+\frac{S_{M_l}}{\rho g^z}\right)\right]+\frac{\partial}{\partial y}[huv]=h\left[\left\{g^x-\frac{u}{|\mathbf{u}|}\mu_\delta g^z-g^z\frac{\partial b}{\partial x}\right\}-M_l u-C_{v_x}u|\mathbf{u}|\right], \tag{10}$$

$$\frac{\partial (hv)}{\partial t}+\frac{\partial}{\partial x}[huv]+\frac{\partial}{\partial y}\left[hv^2+K_y g^z\frac{h^2}{2}\left(1-\frac{S_{M_p}}{\rho g^z}+\frac{S_{M_l}}{\rho g^z}\right)\right]=h\left[\left\{g^y-\frac{v}{|\mathbf{u}|}\mu_\delta g^z-g^z\frac{\partial b}{\partial y}\right\}-M_l v-C_{v_y}v|\mathbf{u}|\right], \tag{11}$$

where b is the basal topography, and $\mathbf{u}=(u, v)$ is the slope-parallel velocity of the moving mass. Equations 9–11 are in conservative form. For practical purposes in higher dimensions, as in Pitman and Le (2005), Pudasaini (2012), and Pudasaini and Mergili (2019), these equations are written in locally varying Cartesian coordinates. This is often preferable in practical applications with advanced computational tools such as r.avaflow (Mergili & Pudasaini, 2024). Note that in practical applications, S_M, M_l, and C_v may be different in the x- and y-directions, depending on the anisotropy of the material and the flow dynamics. The analyses presented above for the geometrically two-dimensional model Equations 6 and 7 also apply for the geometrically three-dimensional dynamic rock avalanche fragmentation model Equations 9–11.

3. Dynamics of Rock-Avalanche Fragmentation

3.1. Numerical Method, Initial Configuration, and Physical Parameters

To explore the fragmentation effect on the spreading and mobility of rock-avalanches, three scenarios are considered here: rock-avalanches with and without fragmentation, and debris avalanches (same material as rock-avalanches but composed of smaller clasts instead of bedrock). From the design of these conditions, our proposed model can reproduce the dynamics of rock-slides without any deformation, rock-avalanches with intensive fragmentation, and rock-avalanches composed of debris with free deformation (means, without any resistance against the deformation induced by the free-surface pressure gradient, Pudasaini & Mergili, 2024). We present a set of simulation results for a landslide down a slope with different resistive forces against the force induced by the hydraulic pressure gradient and the momentum loss at impact. Simulations are performed by numerically solving the unified dynamical model Equations 6 and 7 with the high resolution and very efficient TVD-NOC numerical method (Pudasaini & Hutter, 2007), which has been extensively applied and validated in mass flow simulations with the advanced open source computational tool r.avaflow (Mergili et al., 2017, 2020; Pudasaini & Mergili, 2019; Shugar et al., 2021). Referring to the experiments conducted by Q. Lin et al. (2020, 2022), the traveling path for the simulation consists of an inclined slope at an angle $\zeta = 45°$ from $x = 0$ to $x_a = 350$ m. Then, it continuously transits from $x_a = 350$ m to $x_b = 650$ m decreasing in slope from $\zeta = 45°$ to $\zeta = 0°$ to the horizontal run-out zone. The initial mass of depth $h_0 = 5$ m lies between $x = 40$ m and $x = 60$ m in the upper part of the slope. This mass of bulk density $\rho = 2{,}000$ kgm^{-3} is released with an initial velocity $u_0 = 0$. Following the relevant literature (Pudasaini & Mergili, 2024), the coefficient of viscous drag is chosen as $C_v = 0.002$ m^{-1}. Moreover, the internal and the basal friction angles are $\phi = 33°$ and $\delta = 27°$, respectively.

Before presenting our simulation results, first, we need to specify M_l, S_{M_p} and S_{M_l}. For granular flows or sliding blocks without substantial fragmentation, one may set $M_l \to 0.0$. However, for intense fragmentation, M_l may take a significantly large value (De Blasio & Crosta, 2015; De Blasio et al., 2018). So, subsequent to strong fragmentation we use $M_l = 0.3$ [s^{-1}] for the momentum loss from $x = 400$ m to $x = 460$ m during the impact of the rock mass at the ground, assuming that it takes a while until the major energy loss commences. This represents an inelastic impact. Otherwise $M_l = 0.0$. The typical value of S_{M_p} can be estimated with reference to ρg^z. In the incipient motion, for the material and geometrical parameters given above, as $g^z = g\cos\zeta$, $\rho g^z = 13{,}873$ [kg

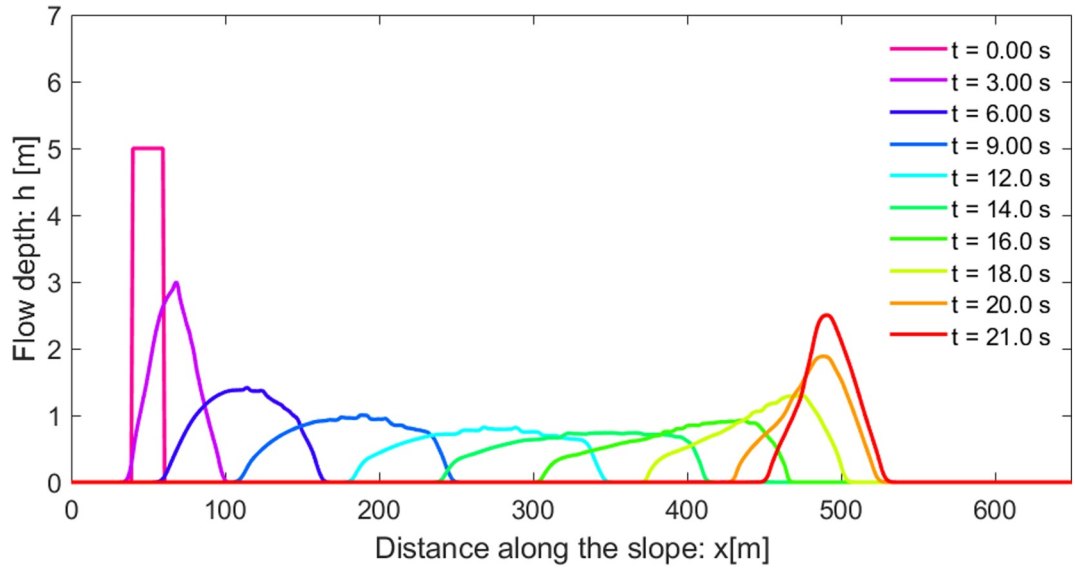

Figure 2. Granular rock avalanche, its slide dynamics and deposition when the momentum loss in the impact is disregarded, and when there is no mechanical control against deformation caused by the pressure gradient.

$m^{-2}s^{-2}$]. Based on this, to apply no deformation control and a strong deformation control, we respectively take $S_{M_p} = 0.0$ and $S_{M_p} = 13{,}422$ [kg $m^{-2}s^{-2}$]. For the fragmentation, due to the intense and strong energy conversion from the elastic strain energy to the enhanced kinetic energy of the rock fragments, from $x_a > 350$, a relatively high value of S_{M_l} is used: $S_{M_l} = 93{,}957[1.0 + (x - x_a)/l]$, $l = 35.0$ m. Here, these values are used for numerical purposes assuming a substantially higher value of S_{M_l}, compared to that of S_{M_p}. This is consistent with the argument presented in Section 2.2.3. However, these values must be scrutinized with laboratory and real-world event data. The linearly slowly increasing value of S_{M_l} describes the higher frontal velocity of the fragmented particles. With these mechanical (strength) parameters, we simulate three scenarios of rock-avalanches. These include a rock-avalanche, a rock-slide, and the dynamics of rock fragmentation with extensive spreading as caused by the mechanically controlled enhanced deformation.

3.2. Results

3.2.1. Granular Rock-Avalanche

Fragmentation can occur at the very beginning of the failure stage of rock-avalanches (Pudasaini & Hutter, 2007). So, the classical model can be applied for the flow of a freely deformable granular mass (Pudasaini & Mergili, 2019). In this situation, the energy loss as the mass impacts the horizontal plane may be considerable or insignificant, whereas the friction and drag can play a major role in energy dissipation. For simplicity, first we consider a rock avalanche composed of a granular mass without any energy loss (due to fragmentation) at the impact (i.e., no energy loss due to impact with the horizontal surface) with $M_l = 0$. The other parameters take the trivial zero values, that is, $S_{M_p} = 0$ and $S_{M_l} = 0$. Figure 2 presents such a granular mass flow down an inclined channel that transits to a horizontal run-out plane at $x = 350$ m. Immediately after the release, the granular mass stretches in downslope direction. As soon as it transits to the horizontal plane, the mass begins to quickly accumulate in the run-out zone due to the basal friction. Such a dynamically changing rock mass deformation happens along the entire flow path, because the mass is assumed to be freely deformable as described by the force induced by the hydraulic pressure gradient, and there is no mechanical control against such deformation ($S_{M_p} = 0$, $S_{M_l} = 0$).

If the energy loss due to the impact is considered, the mass will lose some momentum when entering the transition zone. This will result in the loss of kinetic energy of the flow, decreased run-out, and the associated increased flow depth in the deposition zone. The results are presented in Figure 3 with $M_l = 0.1$ at impact. This is assumed to be a plausible choice for a loose and freely deforming granular flow, because the results indicate that an increase from

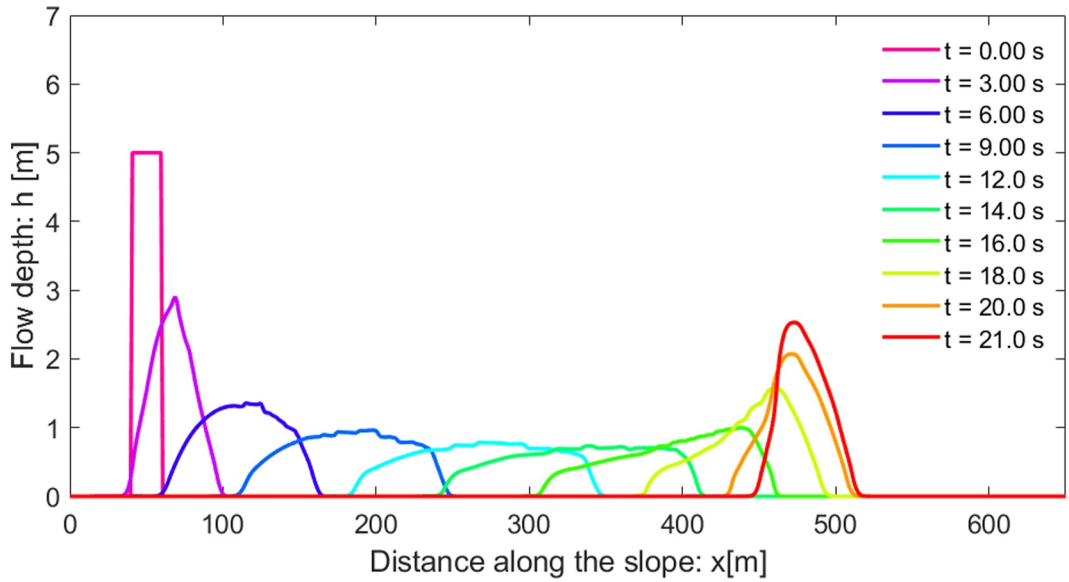

Figure 3. Granular rock avalanche, its slide dynamics and deposition when the nominal momentum loss in the impact is considered, but the mechanical control against deformation caused by the pressure gradient is disregarded.

$M_l = 0.0$ to $M_l = 0.1$ does not lead to a substantial change in the flow dynamics and deposition. In Section 4, we have further increased the value of M_l from $M_l = 0.0$ to $M_l = 0.2$ to analyze how it influences the dynamics of large-scale rock-avalanche fragmentation, and the change is not that substantial. The centers of mass without momentum loss at time t = 16, 18, 20, 21 s are at C_m = 396.00, 447.00, 481.00, and 491.00 m, respectively, whereas with momentum loss, the corresponding centers of mass are at C_m = 395.49, 443.00, 471.87, and 479.38 m. There are some differences between Figures 2 and 3 as the mass transits. However, the difference between Figures 2 and 3 is not that large. This indicates that, for granular flows, the effect of momentum loss at impact may not be very substantial as can be seen from the front and rear positions and the flow depths in these two figures.

3.2.2. Rock-Slide

The second test considers the scenario of a rock-avalanche without fragmentation, which is similar to rock-slide propagation as an intact mass. In this scenario, the rock mass may just slide, virtually without any deformation. The deformation potential caused by the hydraulic pressure gradient is fully controlled by the material strength of the rock mass. Then, the rock mass just translates along the slope and also in the run-out plane virtually without any deformation. Figure 4 depicts this situation with $M_l = 0$, $S_{M_p} = 13,422, S_{M_l} = 0$ as no energy loss in impact is considered, and no fragmentation takes place. Compared with Figure 2 simulating a granular rock-avalanche, the rock-slide dynamics in Figure 4 is fundamentally different from the inception of the motion, through the path to the deposition in the run-out area. The main differences are the geometrical pictures at each time step, the front and the rear positions of the avalanching masses and their extent, the flow depths, and the run-out morphology. Most of these differences can be explained by the mechanical control against the deformation potential associated with the lateral hydraulic pressure gradient.

3.2.3. Rock-Avalanche With Fragmentation

Rock-avalanches with a high degrees of fragmentation display extensive spreading, thin deposits and very high mobility, as field investigations have shown (Crosta et al., 2017; Wang et al., 2018). Fragmentation-induced rapid energy transfer explains these phenomena. There can be different scenarios of fragmentation. One possibility to switch from the controlled motion to fragmentation and the subsequent deformation as a granular flow is when it reaches the transition zone where the impact and fragmentation is intense. This is more likely to happen for huge rock-falls and rock-slides with undulating travel path or abrupt changes in the slope (De Blasio et al., 2018; Strom & Abdrakhmatov, 2018). Previous fragmenting rock-fall and rock-slide experiments and simulations consider

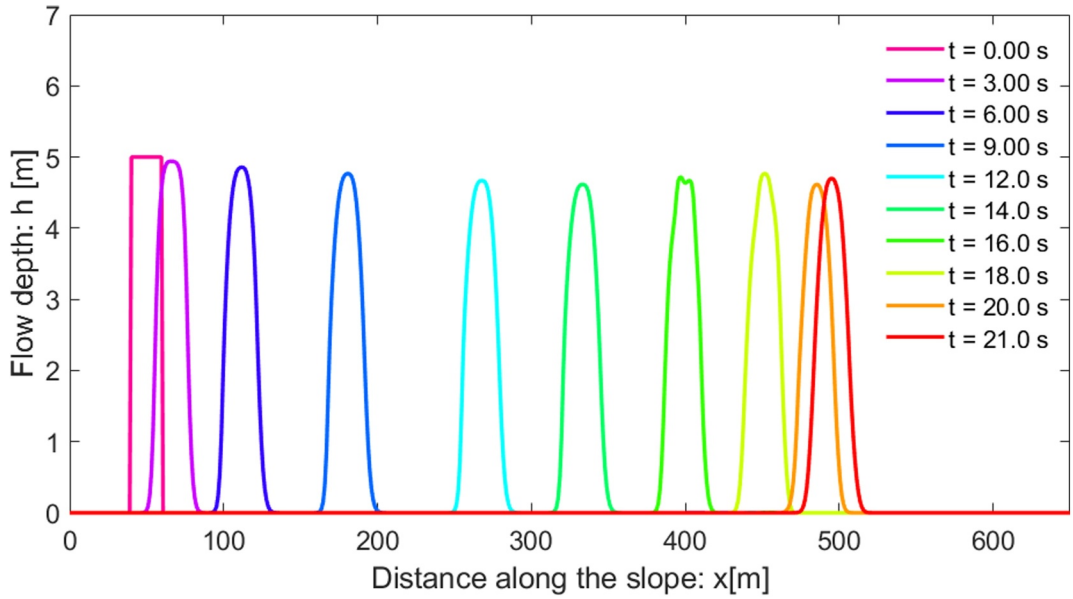

Figure 4. Rock-slide and deposition, virtually without any deformation as the material strength of the rock mass mechanically fully controls the deformation, and the momentum loss due to the impact is disregarded.

this scenario (Bowman et al., 2012; De Blasio & Crosta, 2015; Haug et al., 2016 Q.-W. Lin et al., 2020). In another scenario, the switching can already be considered in the early stage of the motion if the fragmentation already takes place after the rock mass detachment, and if the deformation is substantial. Moreover, disintegration (passive fragmentation) of jointed rock masses cannot invoke such an intense dispersive pressure (McSaveney & Davies, 2006). However, when and how to activate the fragmentation parameter in the simulation is a technical question that should be decided by the practitioner. Here, in the simulation, we mainly focus on the fragmentation following the rock mass impacting the ground in the transition zone. However, in principle, any scenario of the fragmentation dynamics and the subsequent flow of granular rock masses can be simulated by the proposed model Equations 6 and 7. The fragmentation mechanism can be employed through the whole track, or for a given sector of the track even in the run-out zone. All that depends on the particular event and the underlying mechanism. As the avalanching mass continues to impact the ground or local shearing commences, further local fragmentation occurs around this location. The fracturing and fragmentation begins. Then, as the rock fragments completely, the rear material pushes the front part of the mass forward (Q. Lin et al., 2022), transferring the energy from the clasts from the back whose energy is reduced to the frontal clasts. In the meantime, the strain energy stored in the impacting mass is redistributed and released, boosting (enhancing) the velocity of the clasts in the frontal part and reducing the velocity of the clasts in the rear part (De Blasio & Crosta, 2015; Q. Lin et al., 2022).

Here, we consider that the fragmentation starts at the frontal part of the moving mass as it passes through the transition between the inclined plane and the horizontal run-out plane. One possible place at which the rock mass loses the tensile strength is where it impacts the horizontal plane where one can assume that most of the bonds are broken (Haug et al., 2016; Q.-W. Lin et al., 2020).

Here, we focus on the situation where fragmentation takes place as the mass transits from the inclined slope into the run-out area. As the rock mass hits the ground, several important processes happen simultaneously, or in immediate succession: accumulation of the elastic strain energy, fragmentation and the momentum loss of the rock mass, conversion of the stored elastic strain energy into the kinetic energy, generation of the dispersive pressure, and overcoming of the lateral mechanical control (compressional stress). This results in spreading of the fragmented rock particles. The new fragmentation-induced rock avalanche model Equations 6 and 7 includes these aspects through the mechanical parameter S_{M_p} for the mechanical control against deformation, M_l for the momentum loss at impact, and S_{M_l} for the induced lateral pressure. This is the first model of this kind to dynamically simulate the fragmentation process and the subsequent rock-avalanche flow in a unified way.

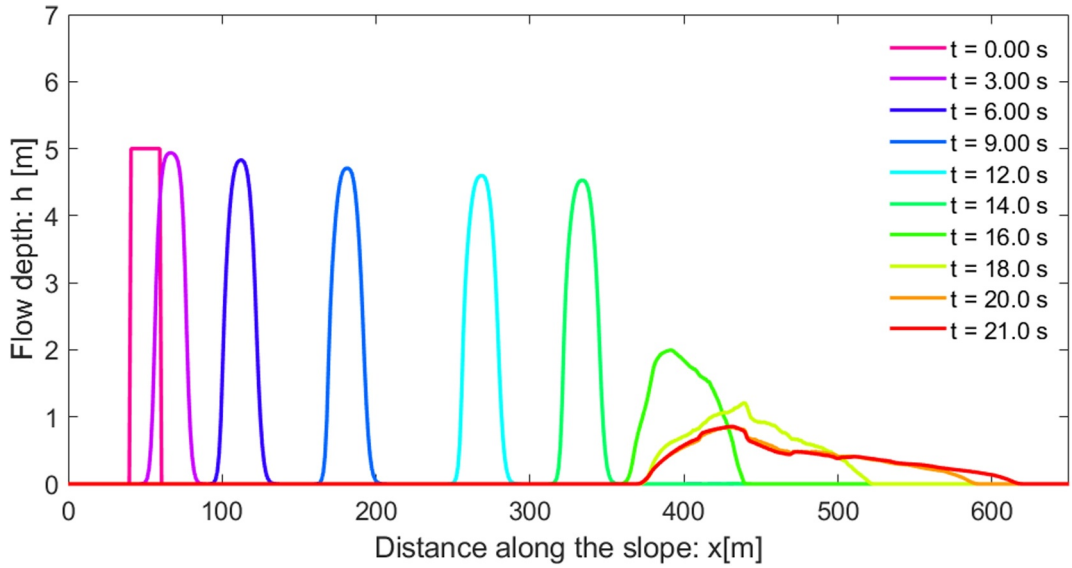

Figure 5. High-intensity fragmented rock-avalanche dynamics, extraordinary spreading, run-out and mobility as the rock mass impacts the ground (transition to the run-out at $x = 350$ m). Initially, the rock mass slides on the inclined slope without any deformation due to its mechanical strength. Momentum loss at impact is considered.

Figure 5 shows the depth evolution of the avalanching mass considering the process of deformation control, momentum loss, overcoming of the tensile strength and the fragmentation after its passage from the inclined slope to the transition into the run-out with parameter values $M_l = 0.3$ (in the region $400 < x < 460$), $S_{M_p} = 13,422$ (for $0 < x < 350$), $S_{M_l} = 93,957[1.0 + (x - 350)/35.0]$ (for $350 < x < 650$). The reason for the choice of these parameters has been explained in Section 3. Otherwise, these parameters are zero. Parameters are selected according to Pudasaini and Mergili (2024) for demonstrating the functionality of the proposed model. For real-world applications, they have to be constrained through field data or laboratory experiments (Q. Lin et al., 2020, 2022). Here, the rock mass slides on the inclined slope until $x = 350$ m, virtually without any deformation as the deformation is fully controlled mechanically by the strength of the rock mass against deformation. Then, as the rock mass enters the transition zone, the mechanical control against deformation is removed, assuming that the tensile strength of the rock mass is overcome by the impact. Overcoming of the tensile strength and removal of the mechanical control can take place synchronously. The rapid overcoming of the tensile strength due to the impact at the ground, that breaks the bonds between the rock elements, and the lifting of the mechanical control against the deformation induced by the hydraulic pressure gradient reflect the dispersive stress effects caused by the high-intensity fragmentation, eventually leading to distal spreading. Then, deposition takes place in the run-out zone. As compared to the fully controlled deformation in Figure 4, now, after $t > 14$ s, the mass begins deforming, first slowly, then faster and faster. The rapid and strong conversion of the strain energy into the kinetic energy results in very intense spreading, thinning, long run-out, and the hypermobility of the propagating granular rock mass. Since the efficiency of fragmentation-induced energy transfer is higher than that of collision-induced energy transfer, dynamic fragmentation enhances the run-out and spreading of rock masses more efficiently than interactions of non-breakable particles during the propagation of rock-avalanches (Q. Lin et al., 2022). Figure 5 reveals this important phenomenon as compared to Figure 4.

Another important observation is that the front of the granular mass flow in Figure 2 moves substantially faster than the front of the rigid rock-slide followed by the fragmented mass in Figure 5 until $t = 16$ s. Thereafter, the front in Figure 2 decelerates and moves slowly because the friction controls the motion in this region. However, in Figure 5, with fragmentation, even with substantial momentum loss during impact, the front of the mass first accelerates rapidly in downstream direction. Only then, it begins decelerating. This resulted in the extraordinary spreading of the mass running out to a tremendous distance with completely different dynamics and morphological features in the deposition fan. Thus, the rock-slides and the fragmented rock mass flows are characteristically different phenomena.

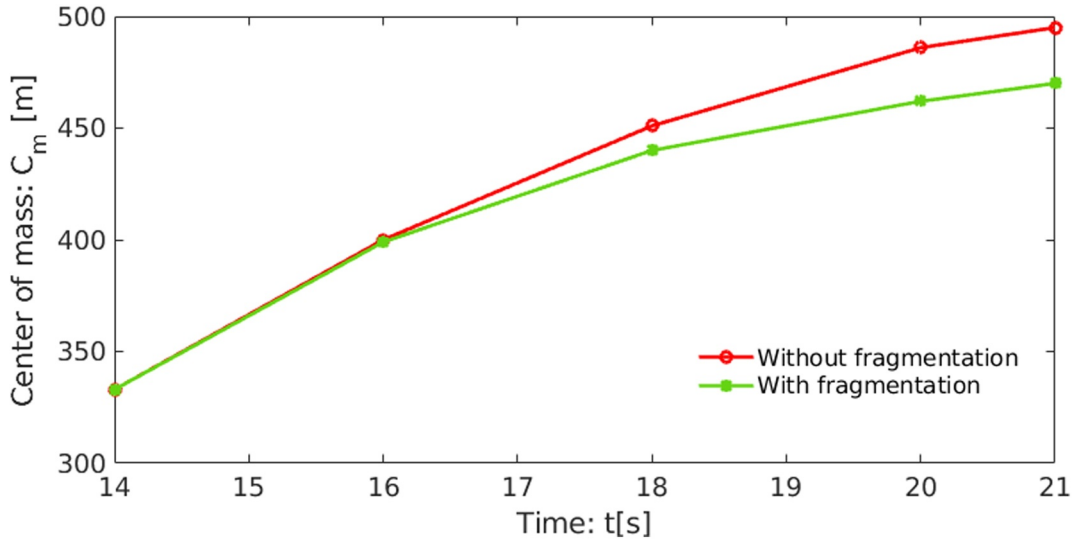

Figure 6. Time evolution of the position of the center of mass without fragmentation and with fragmentation as the fragmentation process begins in the rock-avalanche after $t = 14$ s. With fragmentation, the center of mass is substantially pushed upslope, and this pushing back is intensified with time.

After the transition, the center of mass in Figure 4 without fragmentation is at $C_m = 400$, 451, 486, and 495 m at time $t = 16$, 18, 20, 21 s, respectively. In comparison, the center of mass in Figure 5 with fragmentation is at 399, 440, 462, and 470 m, respectively, at the same time slices. However, note that, in Figure 4 the energy dissipation is a consequence of the basal friction and the drag, but not of the momentum loss at impact. Here, simple basal sliding is considered without fragmentation and deformation. As compared to the non-fragmented rock-slide in Figure 4, in Figure 5 with the high-intensity fragmentation, the center of mass is effectively hindered (by about 1, 11, 25, and 25 m) for the same time slices (after $t = 14$ s) as the mass enters the transition zone to the run-out. The evolution of the center of mass without fragmentation and with fragmentation (including the energy loss as the mass impacts the horizontal plane) are shown in Figure 6 after the fragmentation process begins. The substantially delayed motion of the center of mass when the rock avalanche fragments and moves as a granular flow is clearly shown.

Another important observation from Figure 5 is the highly mobile behavior of the particles (high velocity) in the frontal part and the delayed motion of the particles (low velocity) in the back of the fragmented mass. This is clear from the frontal and the rear position of the rock mass at selected points in time after the fragmentation took place ($t > 14$ s).

The positions of the front, the center of mass and the rear of the avalanche are presented in Figure 7. Until $t = 14$ s, or while the mass slides on the inclined chute, the position of the center of mass lies more or less in the center between the front and the rear positions. However, it is very interesting to observe that, as the rock mass impacts the run-out plane, and the complex fragmentation process commences, the center of mass deviates away from the mid position between the front and the rear of the avalanching granular flow. Although it is moving forward, the center of mass approaches the rear position and moves away from the front position. This can be explained dynamically with the underlying mechanism of the momentum loss in the impact and the fragmentation-induced dispersive pressure. In the rear, a portion of the fragmented mass decelerates and quickly comes to rest, while the frontal part of the mass is pushed much farther away, it spreads and thins in the distal run-out zone. This defines the position of the center of mass.

The velocities of the front, the center of the mass and the rear positions are shown in Figure 8. As the fragmentation takes place and intensifies after $t = 14$ s, although the velocity of the rear position drops rapidly, the velocity of the front increases sharply. However, at this instance, the velocity of the center of mass increases moderately. After $t = 16$ s, as the intensity of the fragmentation decreases, the velocity of the rear continues to drop sharply. A similar behavior, but to a lesser extent, is visible for the velocity of the center of the mass. The decrease of the velocity of the front, however, is much slower than the other two. The rear motion ceases at

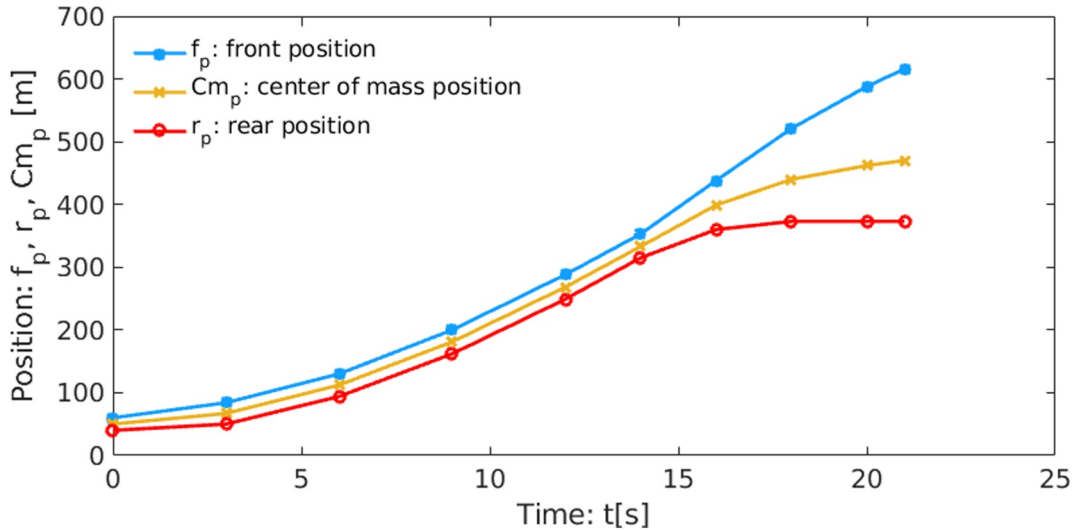

Figure 7. Time evolution of the front, the center of mass and the rear position of the rock-slide with fragmentation.

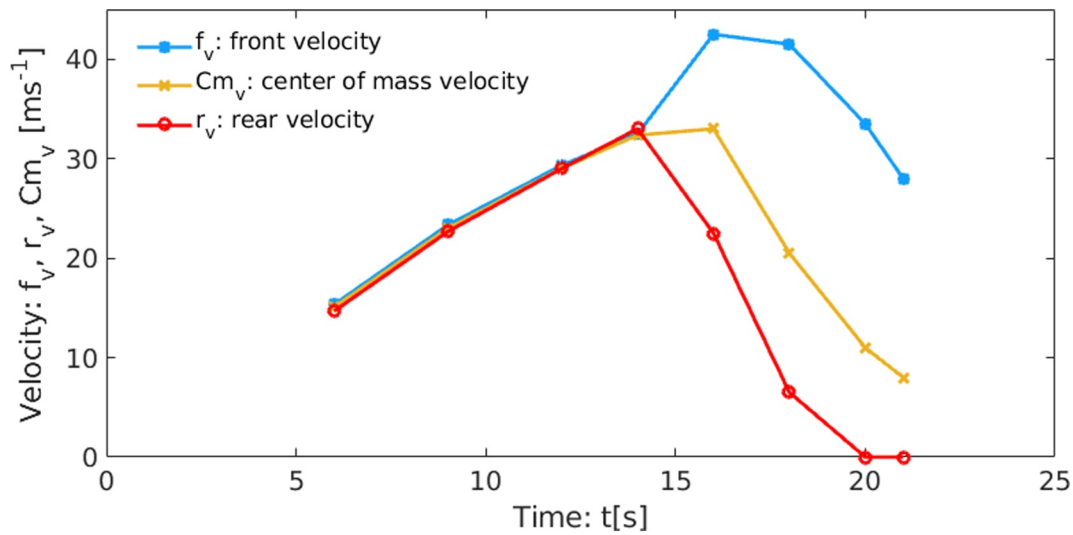

Figure 8. Time evolution of the velocity of the front, the center of mass, and the rear of the rock-slide with fragmentation.

$t = 20$ s, but the center of mass is still moving at a significant velocity. Yet, the velocity of the front is quite high, indicating that its motion continues for quite a while until it comes to a halt.

Next, we dynamically explain what determines the motion of the rear and the frontal portion of the fragmented clasts. After the fragmentation, the clasts have different contributions to the velocities. Upslope from the impact and fragmentation apex, the particle velocity has two contributions, acting in opposite directions. First, the velocity in the forward (downslope) direction follows the momentum of the slide. Second, the dispersive pressure induced by the fragmentation tends to strongly push the clasts in backward (upslope) direction. The resultant of these mutually opposing velocity contributions determines the subsequent motion of these particles, and the morphology of the back side of the deposition. However, the clasts downslope from the impact apex experience two velocity contributions, from the movement from the upslope and the dispersive pressure, both in the forward direction. The resultant of these velocities can be incredibly large, leading to superspreading of the mass in the frontal run-out zone, with rapid thinning of the front in the deposition area. Consequently, the dynamics of the rear and the front determine the position and the velocity of the rear, the center of mass and the front of the avalanching body.

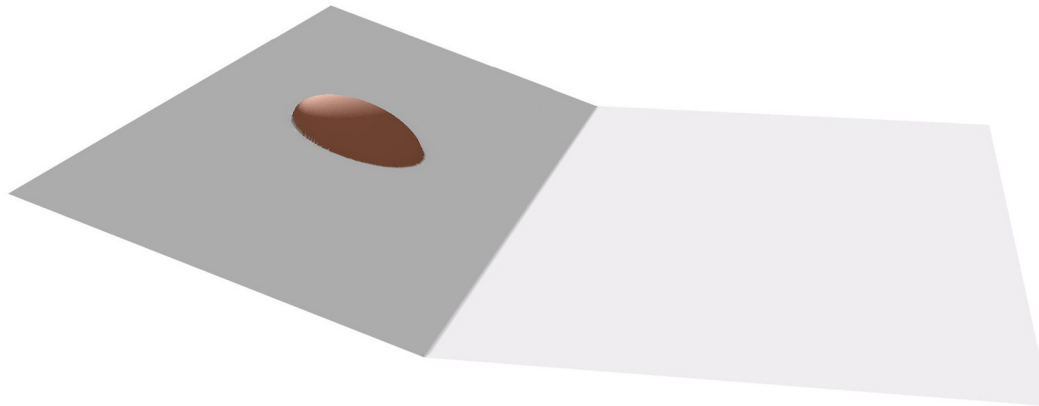

Figure 9. Synthetic landscape (extent 5,000 × 5,000 m) and release mass with a flattened hemispheroid (radius 400 m, maximum height 200 m) used for testing the fragmentation model. Oblique view roughly in positive y direction.

4. Large-Scale Simulations on Synthetic Nature-Oriented Topography

Motivated by the performance of the new model Equations 6 and 7 for small-scale simulations of geometrically two-dimensional motion and deformation of fragmenting rock mass movements, presented in Section 3, we now study the influence of the mechanism of the deformation control, energy loss in impact and fragmentation, and the dispersive lateral pressure on a set of large scale synthetic, geometrically three-dimensional, mass flow simulations with the model Equations 9–11.

4.1. Simulation Set-Up

We apply a series of tests on a synthetic landscape. This landscape, with an extent of 5,000 × 5,000 m, represents a slope in longitudinal (x) direction, and a horizontal run-out plane. The elevation z is calculated as

$$z = \text{if}\left[x < 2100, 700 - \frac{x}{3}, 0\right], \tag{12}$$

where x is the position along the x-axis. A release mass assuming the shape of a flattened hemispheroid with a radius of 400 m and a maximum height of 200 m is centered at the position x = 1,000 m and y = 2,500 m:

$$h = 0.5\sqrt{400^2 - (x - 1000)^2 - (y - 2500)^2}. \tag{13}$$

The setup of the topography and the release mass is illustrated in Figure 9 where the inclined plane is shown in dark-gray color and the horizontal plane is represented in light-gray color.

Our generic case represents a very large rock avalanche, with a volume of 67 million m^3. Landslides of this order of magnitude, and even much larger, have occurred in the past (Legros, 2002; Pudasaini & Miller, 2013). One of the most recent examples of very large rock slope failures is the Daguangbao Landslide in China, triggered by the 2008 Wenchuan Earthquake, with a volume exceeding 1 km^3 (1,000 million m^3) and an initial maximum thickness of 700 m (Cui et al., 2020; Huang et al., 2012). The scar of the 2021 Chamoli Landslide in India (Shugar et al., 2021) displayed a vertical depth of up to 180 m, the same order of magnitude as applied in our generic case. We therefore consider our generic setup representative for a large rock avalanche in nature.

A set of six simulations (Table 1) is performed on the setup illustrated in Figure 9, using the open-source mass flow simulation framework r.avaflow (Mergili & Pudasaini, 2024). In the experiments FR0 − FR3, the fragmentation coefficient C_F is varied, whereas all other parameters are kept constant. C_F [−] is introduced in r.avaflow as a more intuitive and user-friendly alternative to S_{M_l}, in an analogous way to the deformation coefficient C_D [−] (Pudasaini & Mergili, 2024). $C_F = C_D$ would mean that the effects of fragmentation offset the effects of deformation control

Table 1
Parameters for the Computational Experiments Performed on the Setup Shown in Figure 9

Exp./Param.	ρ	ϕ	δ	C_D	C_F	M_l
FR0	2,700	35	16	1.0	**0.00**	0.0
FR1	2,700	35	16	1.0	**2.00**	0.0
FR2	2,700	35	16	1.0	**5.00**	0.0
FR3	2,700	35	16	1.0	**10.0**	0.0
FR6	2,700	35	16	1.0	10.0	**0.1**
FR9	2,700	35	16	1.0	10.0	**0.2**

(C_D). In contrast to C_D, which is always in the range [0, 1], C_F can take values much higher than 1. S_{M_l} is conveniently derived as follows:

$$S_{M_l} = C_F \rho g^z. \tag{14}$$

Substantially higher values of C_F than those of C_D are consistent with the argument that dispersive lateral pressure can be much higher than the compressional pressure mentioned in Section 2.2.3, and considered in the simulation in Section 3.2.3.

In the experiment FR0, fragmentation is generally switched off ($C_F = 0$). In all other experiments, fragmentation is only enabled on the run-out plane, after the moving mass has reached the sudden break of the slope. Fragmentation is disabled on the slope, with a small transition zone in between. Deformation control, in contrast, is generally enabled on the slope, and disabled on the run-out plane. However, these are only some possible scenarios. Fragmentation on the slope would also be possible with enough load above the rock. The experiments FR6 and FR9 investigate the effect of M_l on the momentum loss of the landslide after it has passed the break in the slope and moved onto the run-out plane. Constant values of density ρ [kg m^{-3}], internal friction angle ϕ [°], and basal friction angle δ [°] are applied (Table 1). All simulations are run at a spatial resolution (raster cell size) of 10 m, and stopped after a process duration of 150 s.

4.2. Computational Tool: r.avaflow

r.avaflow (Mergili & Pudasaini, 2023; first introduced in its initial version by Mergili et al., 2017) represents a comprehensive open-source computational framework for the simulation of gravitational mass flows. It is most efficiently run as an extension to the GIS software GRASS. The multi-phase, multi-mechanical, flexible model introduced by Pudasaini and Mergili (2019) is used to route different types of mass flows (such as rock avalanches, flow-type snow avalanches, debris flows, or floods) down a natural or generic topography. The multi-phase model is also particularly suitable for the simulation of complex geomorphic process chains such as glacial lake outburst floods (Mergili et al., 2020). The model equations are solved through a TVD-NOC numerical scheme (Pudasaini & Hutter, 2007). r.avaflow offers various additional functionalities such as entrainment, stopping, or hydrograph input, all out of scope here, and therefore not considered in the present model simulations.

For the present work, the multi-phase model (considering coarse particles, fine particles and viscous fluid with fundamentally different physical properties and mechanical responses) (Pudasaini & Mergili, 2019) used in r.avaflow is equipped with the controlled deformation, momentum loss in impact and dispersive pressure model introduced in Section 2, considering only the first (solid) phase.

4.3. Results

Applying the dynamic rock-avalanche fragmentation model Equations 9–11, we now present and analyze the simulation results based on three important aspects controlling the motion and deformation, run-out and deposition of the landslide. These are the mechanically controlled deformation, momentum loss during impact, and the dispersive lateral pressure.

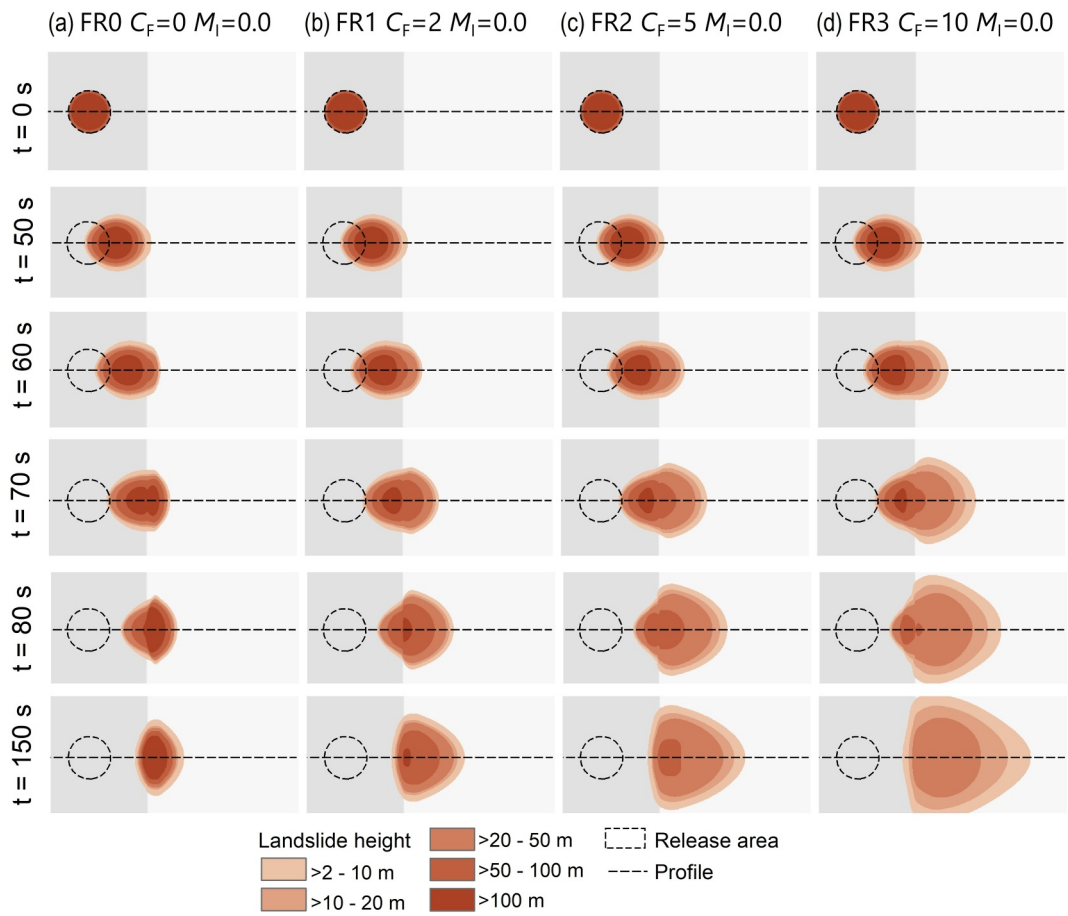

Figure 10. Evolution of the landslide flow height for four selected numerical experiments. The radius of the release mass (indicated by the dashed circle) is 400 m, providing the scale. The dashed lines indicate the longitudinal profile lines used to generate Figure 11 for the landslide height profiles. FR0 − FR3 are the simulation experiments. The deformation control C_D is activated on the inclined plane (on the left side). The fragmentation coefficient C_F is activated on the horizontal plane (in the right). The momentum loss during impact M_l is de-activated.

4.3.1. Mechanically Controlled Deformation

In all the simulation results presented in Figures 10–13, a strong mechanical control against the deformation induced by the hydraulic-pressure gradient is applied on the entire inclined surface (indicated by left dark-gray plane in Figures 10 and 12). This models a largely intact rock mass until about $t = 50$ s. Except for some unavoidable numerical diffusion, the moving mass slides down the slope without deformation. As the mass impacts the horizontal run-out plane ($t \geq 50$ s), the mechanical control against the deformation is removed, allowing the rock mass to freely deform in the transition and the run-out zone, as well as in the deposition zone (indicated by the right light-gray plane in Figures 10 and 12).

4.3.2. Spreading Caused by Dispersive Lateral Pressure

4.3.2.1. Ground Plot Evolution

One of the major aspects in rock-fragmentation and subsequent dynamics is associated with the fragmentation-induced dispersive pressure resulting in the spreading of the fragmented rock clasts. To model such dynamics, we apply different dispersive lateral pressure parameter values for S_{M_l}. The results are depicted in Figure 10. Panel (a), FR0, is without dispersive lateral pressure $C_F = S_{M_l}/(\rho g^z) = 0$, and is considered as the reference for analysis. As the mass transits from the inclined plane to the horizontal plane ($t \geq 50$ s), it starts deforming substantially due to the force associated with the hydraulic-pressure gradient, because the deformation control is removed. In this region, the moving mass behaves as a granular material. As the basal friction is the main energy

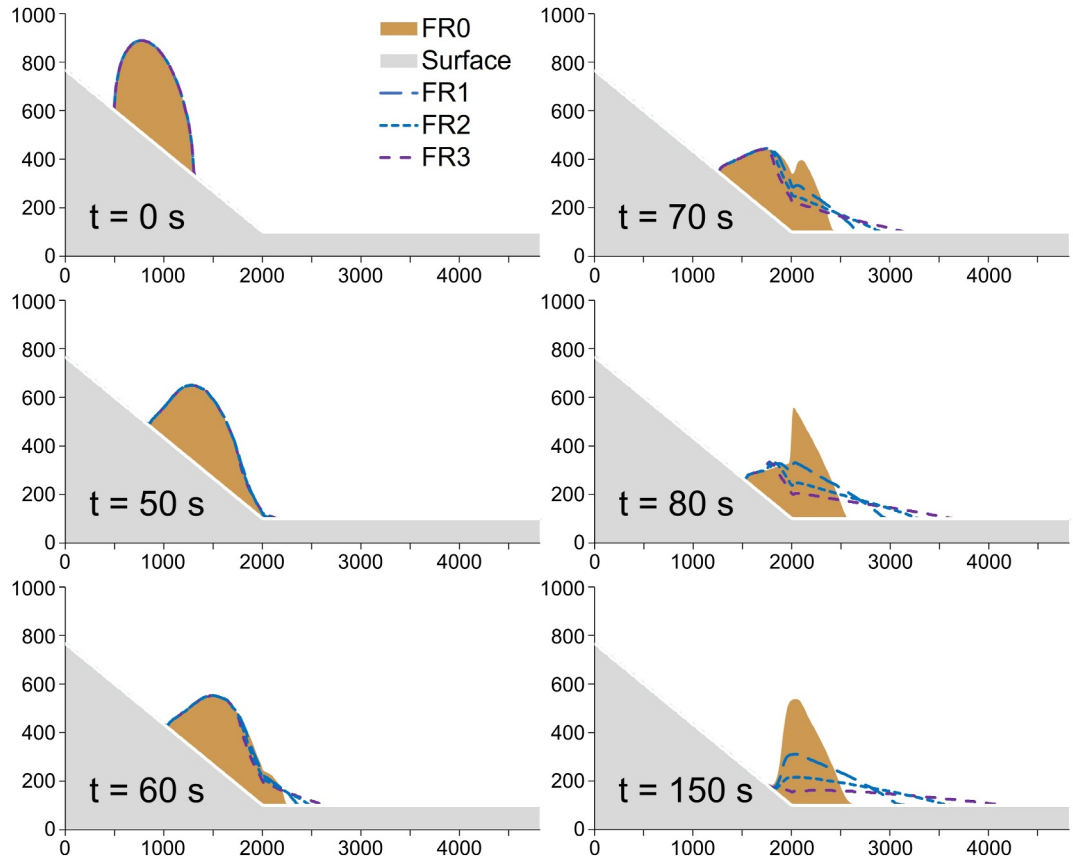

Figure 11. Flow height evolution for four selected experiments (Table 1) and six selected points in time, along the longitudinal profile illustrated in Figure 10. Note that the aspect ratio is out of scale. For better visualization, the flow height is 2-fold exaggerated; offset: x-axis by −100 m, z-axis by 100 m.

dissipation mechanism and the gravitational acceleration is zero in the run-out plane, the mass deforms more in the transversal direction than in the longitudinal direction. The mass quickly starts accumulating just beyond the slope break ($t \geq 70$ s), and finally comes to a standstill at $t = 150$ s, within a narrow area.

The situation becomes more interesting as we apply and increase the dispersive lateral pressure parameter values for C_F from $C_F = 2$ (panel (b), FR1) to $C_F = 10$ (panel (d), FR3). The most spectacular dynamics and spreading is shown with $C_F = 10$ (panel (d), FR3). As soon as the mass impacts the ground ($t \geq 60$ s), due to the fragmentation induced dispersive lateral pressure, the mass starts to spread radially outwards in all (plane) directions. The fragmented granular mass thins outward forming the tapered structure. This effect is much stronger with $C_F = 10$ (panel (d), FR3) than with $C_F = 5$ (panel (c), FR2), or $C_F = 2$ (panel (b), FR1).

4.3.2.2. Profile Evolution

Detailed and better dynamical and local information can be acquired by looking at the profile evolution along the central line of the flow in the downslope direction as extracted from Figure 10. The results are presented in Figure 11. Again, FR0 (with $C_F = 0$) is considered as the reference for the analysis against the higher values of the dispersive pressure. In this situation, as the mass impacts the plane surface and the deposition process begins (after $t \geq 60$ s), we observe that, due to the vanishing gravitational acceleration and dominant basal friction, the rapidly descending front starts decelerating swiftly. As the frontal portion of the mass can now deform on the run-out plane, it quickly develops into the surging front, in contrast to the still largely intact mass behind on the inclined slope ($t = 70$ s). The strong pushing from the upper portion (solid-type) of the large mass, and the firm frictional resistance from the front, result in the momentarily very sharp peak at around $t = 80$ s. As time proceeds, the sharpness of this peak diffuses, it becomes more gently curved. The mass has deposited at $t = 150$ s with most of it lying in the run-out zone, whereas some portion remains on the inclined slope.

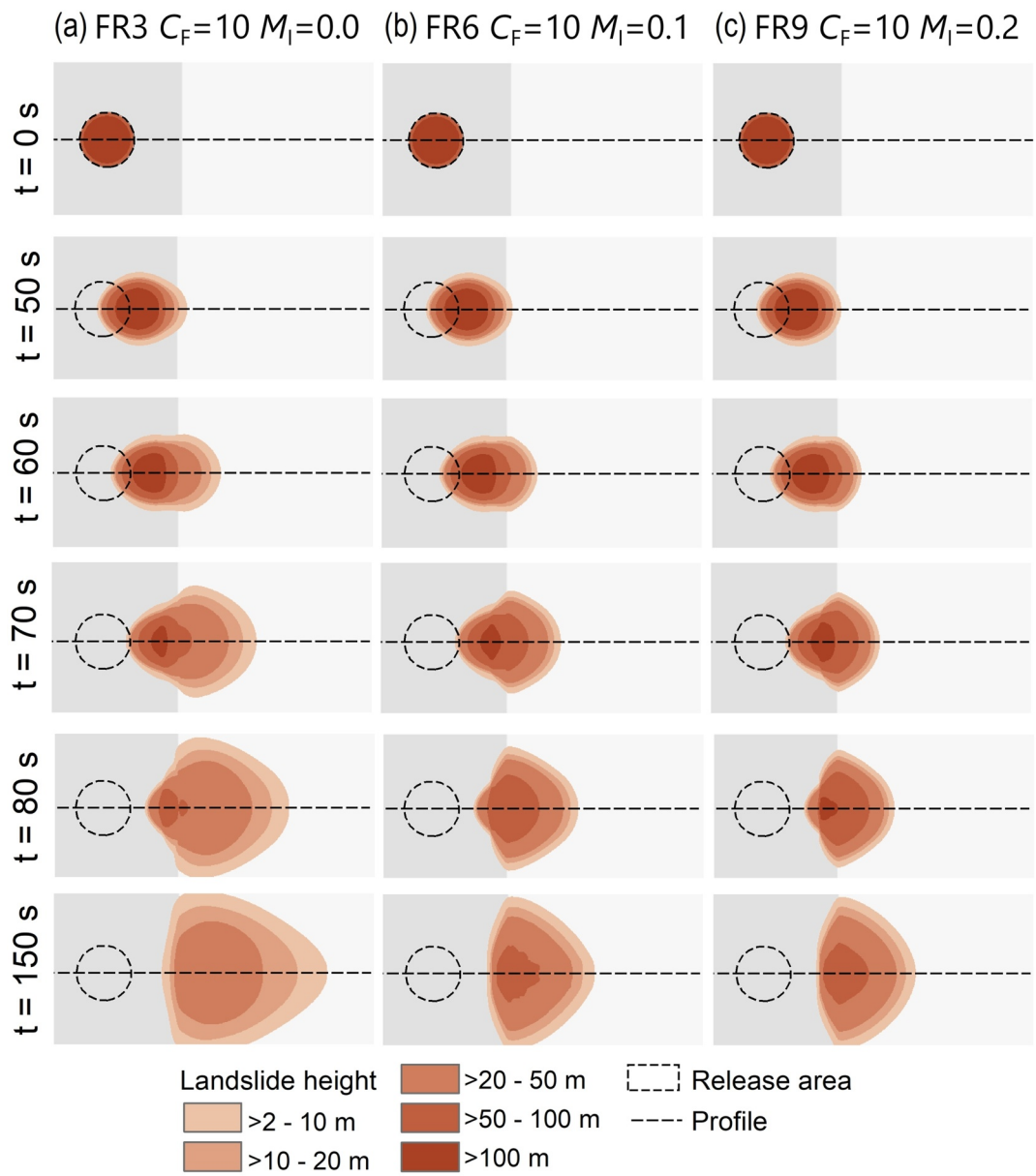

Figure 12. Evolution of the landslide flow height for three selected numerical experiments. The radius of the release mass (indicated by the dashed circle) is 400 m, providing the scale. The dashed lines indicate the longitudinal profile lines used to generate Figure 13 for the landslide height profiles. FR3 – FR9 are the simulation experiments. The deformation control C_D is activated on the (left) inclined plane. The momentum loss during impact M_l and the fragmentation coefficient C_F are activated on the horizontal plane on the right side.

We now focus on the more interesting situation when the dispersive pressure is employed, with C_F = 2, 5, 10, corresponding to FR1, FR2 and FR3. With the highest value of the dispersive pressure in FR3, we observe that, already at t = 60 s, the front propagates substantially away from the inclined slope. Because the strong fragmentation starts at the slope break, the frontal portion of the mass on the run-out plane is fluidized. So, no sharp front as in FR0 can form after t = 60 s. Rather, the moving mass quickly spreads out in a progressively thinning outward front, and eventually comes to rest at t = 150 s. Probably the most important information can be gathered from the comparison of the deposition patterns among the simulations with FR0, FR1, FR2, and FR3. As compared with FR0, the frontal position for FR3 is approximately 1,500 m farther away from the slope break, which is a huge difference. The fronts simulated in the experiments FR2, FR1, and FR0 are very much behind. The maximum flow height decreases quickly from FR0 to FR1 and, at a lower rate, from FR1 to FR2 to FR3.

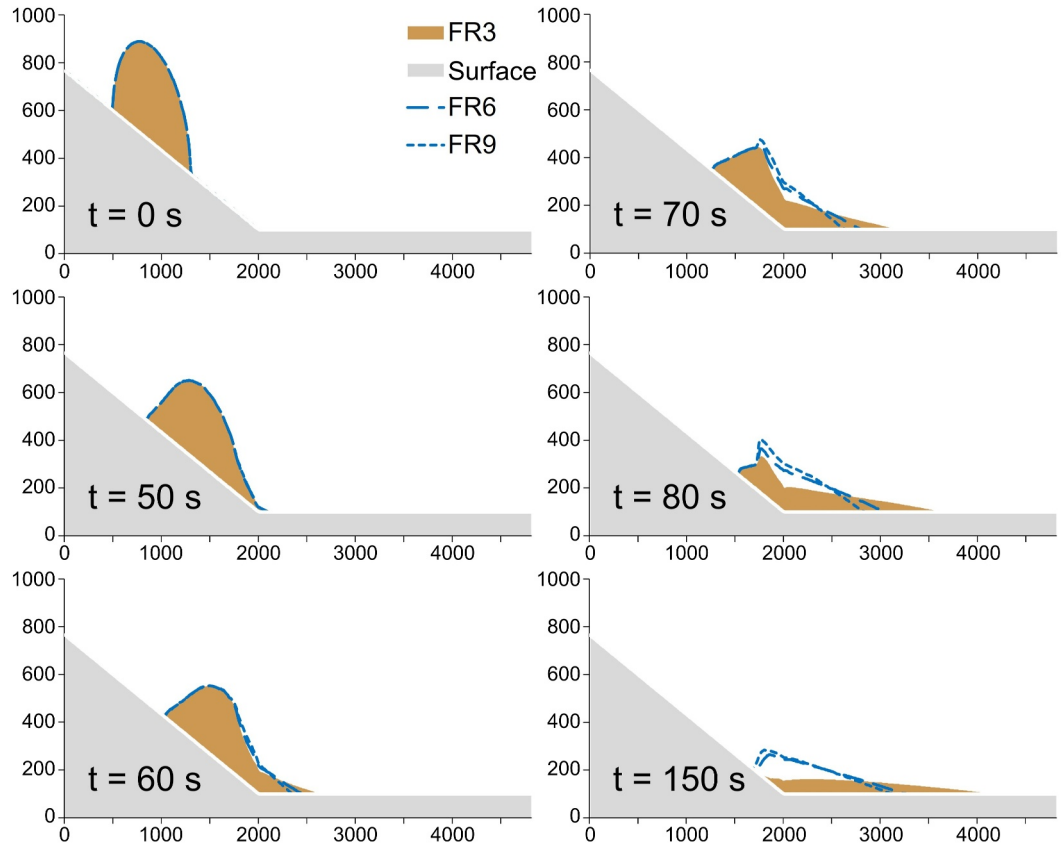

Figure 13. Flow height evolution for all three experiments (Table 1) and six selected points in time, along the longitudinal profile illustrated in Figure 12. Note that the aspect ratio is out of scale. For better visualization, the flow height is 2-fold exaggerated; offset: x-axis by −100 m, z-axis by 100 m.

Thus, the fragmentation-induced lateral dispersive pressure plays a fundamental role in the overall mass transport, transition and deposition of the fragmented rock clasts.

4.3.3. The Control of the Momentum Loss During Impact

4.3.3.1. Ground Plot Evolution

Another crucial aspect of fragmenting rock-avalanches is the energy loss as the rock mass experiences a suddenly decreasing slope (here, impacting the horizontal plane). Part of the momentum carried by the moving mass is consumed during impact. Depending on the intensity of the momentum loss in this process, the subsequent dynamics may change substantially to strongly. The results are presented in Figure 12 for different values of momentum loss. For this, we consider FR3 (from Figure 10d) as a reference, and apply $M_l = 0.1$ and $M_l = 0.2$ (FR6 and FR9, respectively) for the simulations with 10% and 20% momentum loss. We analyze the situation with FR9. As soon as the mass impacts the ground ($t \geq 50$ s) in panel (c), spreading and the propagation speed are controlled. The overall control of the momentum loss in mass propagation and spreading during transition, run-out, and deposition can be accessed by looking at the final morphology of the deposit at $t = 150$ s. The mass spreading during deposition for FR3 is quite intense, whereas the mass spreading in FR9 is substantially controlled, that is, the deformation and propagation are radially restricted due to the momentum loss, as can be seen by comparing panel (c) with panel (a). However, the change between FR6 and FR9 is less than the change between these and FR3. This means that even a small amount of momentum loss can exert a strong effect on the dynamics and deposition of the fragmenting rock avalanche. As no mass impact at the ground, and no fragmentation can take place without momentum loss, we emphasize that proper models and simulations of the mass transport require inclusion of the momentum loss.

4.3.3.2. Profile Evolution

For a better understanding of the main characteristics of the mass transport, it is preferable to analyze the dynamics, run-out and deposition along the central flow line. The results are shown in Figure 13. As before, we focus for the motion after $t \geq 50$ s (for FR9). With the energy (or the momentum) loss in impact during fragmentation, the propagation speed is immediately and strongly reduced as can be seen for $t \geq 70$ s. This results in a substantially increased flow height with a type of folding, already before the transition, yet strongly reduced travel distance. This effect is clearly seen in the deposition profiles at $t = 150$ s. As compared to FR3, the reduction of the run-out length in FR9 is about 1,000 m, demonstrating the importance of the momentum loss. Another key observation is that, because of the momentum loss at and after the slope break, the motion, mainly in the back, is delayed. Consequently, a substantial fraction of the mass now remains on the inclined slope. However, as shown in Figure 13, the difference between FR6 and FR9 is minimal.

The results presented in Section 3 and in this section are in line with the phenomena observed in laboratory experiments and real-world events of rock fragmentation and the subsequent flow dynamics. This indicates that the proper modeling and implementation of the associated aspects of mechanically controlled deformation, energy loss in impact, fragmentation induced dispersive pressure and earth pressure is essential for the purposeful simulation of dynamic rock fragmentation and its effects on the overall behavior of rock-avalanches. Three-dimensional animations of the experiments FR0–FR9 are included in Supporting Information S1.

5. Discussion

There are five important aspects in our unified dynamic simulation model for the fragmentation-induced avalanching motion of rock mass movements. First, the deformation of the rock mass is mechanically controlled until it disintegrates and flows as a granular mass. Second, we introduced an intensive momentum loss during the impulsive impact by the rock mass at a slope of lower inclination (in our test cases, a horizontal run-out plane). Third, as the impact and disintegration process overcomes the tensile strength of the rock mass, the mechanical control against the deformation is removed. Fourth, synchronously, the elastic strain energy converts into the kinetic energy that is combined with the force associated with the lateral pressure gradient as the dispersive pressure, enhancing the frontal motion and distal spreading. Fifth, all these mechanical processes can be controlled locally. We have, therefore, presented a unified and flexible model for the dynamic simulation of rock slides, their fragmentation, and the resulting avalanching motion with substantial thinning, spreading, and extraordinary mobility in the run-out zone.

With the fragmentation-induced rock avalanche model Equations 6 and 7, we obtained some interesting and meaningful results. First, velocity boosting (enhancing, De Blasio & Crosta, 2015) of the frontal mass caused by impact-fragmentation is consistent with laboratory experiments (Bowman et al., 2012; Haug et al., 2016; Q.-W. Lin et al., 2020; S.-L. Zhang et al., 2023). It implies that the new model captures some essential features of the experimental phenomena of rock mass movements and fragmentation dynamics. Second, as shown in Figure 5, the profile of deposition considering the rock fragmentation displays a much higher degree of spreading with the deposited mass being thinner compared to the simulation without considering fragmentation. Such a highly spreading feature is similar to that observed in real-world rock avalanches, which are usually characterized by wide and thin deposits (Strom & Abdrakhmatov, 2018; Wang et al., 2018).

We would like to emphasize that our conclusions on the plausibility of the simulation results build on the qualitative analysis of the variation of the fragmentation parameters, which are evaluated against our physical understanding of the governing processes rather than against empirical evidence. The latter would be a challenging task due to mixed effects of different phenomena and parameters (friction, fragmentation, deformation, energy loss through shearing, etc.), and the resulting equifinality issues. This requires further research on this topic.

We note that the dispersive pressure was also included in the simulation model by T. R. Davies and McSaveney (2002). However, in their model it was considered as a parameter by linearly increasing the earth pressure parameter by the same amount for the active and passive states. Here, we do not impose any condition on the earth pressure parameter, which evolves dynamically as determined by the state of motion, described by Equation 4. Rather, the dispersive pressure is modeled separately by introducing the dispersive pressure parameter S_{M_l} that can have any form. We hypothesize that the lateral pressure due to fragmentation evolves (amplified or de-

amplified) automatically when the material is in the active or passive state without imposing any condition on it. Moreover, while T. R. Davies and McSaveney (2002) used the same dispersion effect down the entire slope, we distinguish different local sections of the flow path as mechanically controlled sliding zone, impact zone, energy conversion and dispersion zone, and the distal zone without any of these effects. Such a zoning can more realistically capture the main fragmentation process of real-world events. However, the zoning depends on specific situations of the rock avalanche, and has to be determined for each case individually.

The new model Equations 6 and 7 can also be applied to better simulate the influence of fragmentation on the dynamics of multi-phase mass flows. This includes phenomena such as the devastating Piz-Cengalo Bondo (Mergili et al., 2020) and Chamoli (Shugar et al., 2021) rock-ice avalanche events. Both have previously been simulated with the multi-phase mass flow model of Pudasaini and Mergili (2019), but without considering the mechanism of fragmentation. As these, and also the Bliggspitze rock-ice avalanche (Pudasaini & Krautblatter, 2014), involve intense fragmentation of the rock and the ice elements involved in the dynamic motion, it is logical to assume that they can be better simulated by employing the new mechanisms associated with fragmentation, energy loss, energy conservation, and dispersive pressure, by embedding these principles into the multi-phase mass flow model by Pudasaini and Mergili (2019). The mechanism of the mass and momentum transfer in rock-ice mixtures, following the principles introduced by Pudasaini and Krautblatter (2014) and Pudasaini (2024), should be included, too. Another important aspect is that, as strong fragmentation takes place, it converts the previously intact rock mass into finer and coarser rock particles. With the fragmentation, we should better couple the single-phase simulation model to the two- or multi-phase simulation model (Pudasaini & Mergili, 2019) in which particles of different physical properties (grain size, density, friction, viscosity, etc.) can be considered as different phases. In the subsequent granular mixture flow, the particles of different physical properties tend to separate from one another. Here, the mechanical phase separation model proposed by Pudasaini and Fischer (2020) can be applied to describe the phase separation phenomenon in mixture mass flows. Only some main aspects of fragmentation are simulated here. For real-world rock-slides and rock-avalanches, the rock fragmentation process may continue until the avalanche mass finally stops, particularly the shear-induced fragmentation in the basal layer. So, the shear-induced fragmentation should be embedded into the proposed model.

The discussion presented above for the geometrically two-dimensional model Equations 6 and 7 also applies to the geometrically three-dimensional dynamic rock-avalanche fragmentation model Equations 9–11. Evaluation of the model against laboratory experiments and real-world events will be an important further task which, however, is out of scope here.

Fragmentation is one of several possible mechanisms for the enhanced flow mobility of rock-avalanches. The other agents of mobility may include the excess volume, fine particles or powders along the sliding surface, interstitial fluids and pore fluid pressure, air pockets, collisions between particles, steam generation, melting of the particles, basal lubrication and internal fluidization, and the entrainment of bed material. Further details on this can be found in Legros (2002), Pudasaini and Miller (2013), Pudasaini and Krautblatter (2021), and Cagnoli (2024).

As reported in the literature, fragmentation is a pervasive phenomenon in rock-avalanches and was proposed as one possible mechanism for the extremely high mobility of rock-avalanches. However, due to the destructive capacity of rock-avalanches, direct observations on rock-avalanche emplacement are rare, which greatly limits the research on the fragmentation effect of rock-avalanches. In recent years, the fragmentation process of rock-avalanches was studied by simplified laboratory tests and it is argued that fragmentation is an energy consume process and only can enhance the runout of the frontal part. Therefore, the contribution of fragmentation on the mobility of rock-avalanches is still in debate. Additionally, different processes and hypotheses have been proposed to explain the high mobility of rock-avalanches with the finding of different geological evidence, which indicates that the propagation process of rock-avalanches is complex. For example, the increase of volume, generation of fine particles along the sliding surface, mineral melting, entrainment of bed material, and particle collisions are all possible reasons controlling the mobility of rock-avalanches. Each of the processes mentioned above may operate synchronously, but some of the processes may dominate the others. In principle, each of these processes may be connected to other processes with the possibility of feedback, and thus, altering the flow dynamics, runout and deposition. As the interactions between these aspects are complex, a detailed consideration would go far beyond the scope of this paper.

However, we mention that the entrainment of bed material can enhance the flow mobility (Pudasaini & Krautblatter, 2021) with two immediate consequences: high impact force and higher momentum loss at impact. Conversely, as the fragmentation alters the dynamics of the frontal and the rear of the sliding mass, the entrainment rates in these regions are also altered depending on the locally applied shear loads. Moreover, fragmentation produces coarse and fine particles with differing physical and rheological properties. Soon after fragmentation, the flow often results in phase separation or particle sorting (Pudasaini & Fischer, 2020). As the finer particles dominate the bottom and the rear of the flow, here the (shear-induced) fragmentation process may be weak or negligible. Whereas, since the top, and particularly the front, are dominated by coarse particles, here, even in the later stage of motion, the fragmentation process may still play a significant role. Thus, as the fragmentation amplifies the phase separation process, this, in turn, changes the local fragmentation dynamics.

The comprehensive principle of rock-avalanche fragmentation and associated dynamics can be viewed as a novel and unified explanation for super-spreading and long run-out. The fragmentation-induced velocity boosting is a crucial addition to our understanding of rock-avalanches. Mechanically, there is stronger evidence for the results presented here in explicitly explaining the hyper-mobility and extraordinarily thinning run-out than for the other processes mentioned above. However, the proposed principle should be scrutinized and validated.

6. Conclusions

We proposed a novel, unified and flexible mechanical model for the dynamic simulation of fragmentation in rock mass movements, and the motion of the resulting avalanching flows. The simple physically based model relies on the mechanically controlled landslide deformation principle, energy loss at impact, and energy conversion during fragmentation. Our analysis reveals that there are three mechanical processes of fundamental importance associated with the fragmentation and subsequent dynamics of rock mass movements. First, the mechanical control against deformation. Second, the momentum loss at impact. Third, the fragmentation-induced impulsive evolution associated to the lateral pressure. All these effects play important roles in controlling the deformation, spreading, and hypermobility in the run-out zone. The newly introduced, unified dynamical principle describes the fragmentation-induced energy transfer leading to a larger kinetic energy increase in the frontal material and less energy loss in the entire moving mass. This leads to an energized and enhanced forward movement of the frontal material, a reduced mobility of the rear portion of the propagating rock-avalanche, and the lagged position of its center of mass, as compared with non-fragmenting rock-avalanches. The analysis of the results shows very interesting and important features of and mechanical insights to the fragmentation dynamics, spreading, run-out, and deposition morphology. These results are in line with observations in the field and with laboratory experiments. The new model addresses the long-standing question of dynamically simulating the fragmentation of rock mass movements, and the propagation and wide-spread deposition of the resulting rock-avalanches, in a mechanically controlled way. This demonstrates the mechanical strength of our new dynamic rock-avalanche fragmentation model and its potential for more realistic simulations of real-world events.

Acknowledgments
We sincerely thank the Editor Amy East, Associate Editor Matt Brain, and Reviewers for their constructive comments and suggestions that helped to substantially increase the clarity and quality of this paper. Shiva P. Pudasaini: Acknowledges the financial support from the German Research Foundation (DFG) through the research project: "Landslide mobility with erosion: Proof-of-concept and application —Part I: Modeling, Simulation and Validation"; Project number 522097187. Martin Mergili: This work is part of the project "Moving mountains—landslides as geosystem services in Austrian geoparks" (ESS22-24—MOVEMONT) funded through the Earth System Sciences programme of the Austrian Academy of Sciences. Qiwen Lin and Yufeng Wang: This research has been supported by the National Natural Science Foundation of China (Grants 41941017 and 42207203). Open Access funding enabled and organized by Projekt DEAL.

Conflict of Interest

The authors declare no conflicts of interest relevant to this study.

Data Availability Statement

The large-scale simulations were performed with an enhanced version of r.avaflow 3G. Instructions on how to install and run the software can be found on the r.avaflow website https://www.avaflow.org (Mergili & Pudasaini, 2024). The shell script has to be executed to generate the input data and to run the simulations (to be used on Linux, preferably Ubuntu 20.04LTS, within GRASS 7.8 or GRASS 8). The script can be found at Pudasaini et al. (2024).

References

Bagnold, R. A. (1954). Experiments on a gravity-free dispersion of large solid spheres in a Newtonian fluid under shear. *Proceedings of the Royal Society of London A*, *225*, 49–63.

Bowman, E. T., Take, W. A., Rait, K. L., & Hann, C. (2012). Physical models of rock avalanche spreading behaviour with dynamic fragmentation. *Canadian Geotechnical Journal*, *49*(4), 460–476. https://doi.org/10.1139/t2012-007

Cagnoli, B. (2024). Flow front mobility of rock avalanches as a function of flow volume, grain size, channel width, basal friction and flow scale. *Landslides*, *21*(5), 933–947. https://doi.org/10.1007/s10346-023-02190-9

Cagnoli, B., & Quareni, F. (2009). Oscillation-induced mobility of flows of rock fragments with quasi-rigid plugs in rectangular channels with frictional walls: A hypothesis. *Engineering Geology*, *103*(1–2), 23–32. https://doi.org/10.1016/j.enggeo.2008.07.009

Choi, C. E., & Goodwin, S. R. (2021). Effects of interactions between transient granular flows and macroscopically rough beds and their implications for bulk flow dynamics. *Canadian Geotechnical Journal*, *58*(12), 1943–1960. https://doi.org/10.1139/cgj-2020-0160

Collins, G. S., & Melosh, H. J. (2003). Acoustic fluidization and the extraordinary mobility of sturzstroms. *Journal of Geophysical Research*, *108*(B10), 2473. https://doi.org/10.1029/2003JB002465

Crosta, G. B., Hermanns, R. L., Dehls, J., Lari, S., & Sepulveda, S. (2017). Rock avalanches clusters along the northern Chile coastal scarp. *Geomorphology*, *289*, 27–43. https://doi.org/10.1016/j.geomorph.2016.11.024

Cui, S., Yang, Q., Pei, X., Huang, R., Guo, B., & Zhang, W. (2020). Geological and morphological study of the Daguangbao landslide triggered by the Ms. 8.0 Wenchuan earthquake, China. *Geomorphology*, *370*, 107394. https://doi.org/10.1016/j.geomorph.2020.107394

Davies, T., McSaveney, M., & Kelfoun, K. (2010). Runout of the Socompa volcanic debris avalanche, Chile: A mechanical explanation for low basal shear resistance. *Bulletin of Volcanology*, *72*(8), 933–944. https://doi.org/10.1007/s00445-010-0372-9

Davies, T. R., & McSaveney, M. J. (2002). Dynamic simulation of the motion of fragmenting rock avalanches. *Canadian Geotechnical Journal*, *39*(4), 789–798. https://doi.org/10.1139/t02-035

Davies, T. R., & McSaveney, M. J. (2009). The role of rock fragmentation in the motion of large landslides. *Engineering Geology*, *109*(1–2), 67–79. https://doi.org/10.1016/j.enggeo.2008.11.004

Davies, T. R., McSaveney, M. J., & Hodgson, K. A. (1999). A fragmentation spreading model for long-runout avalanches. *Canadian Geotechnical Journal*, *36*(6), 1096–1110. https://doi.org/10.1139/t99-067

Davies, T. R. H. (1982). Spreading of rock avalanche debris by mechanical fluidization. *Rock Mechanics*, *15*(1), 9–24. https://doi.org/10.1007/bf01239474

Davies, T. R. H., Reznichenko, N. V., & McSaveney, M. J. (2020). Energy budget for a rock avalanche: Fate of fracture-surface energy. *Landslides*, *17*(1), 3–13. https://doi.org/10.1007/s10346-019-01224-5

De Blasio, F. V., & Crosta, G. B. (2015). Fragmentation and boosting of rock falls and rock avalanches. *Geophysical Research Letters*, *42*(20), 8463–8470. https://doi.org/10.1002/2015GL064723

De Blasio, F. V., Dattola, G., & Crosta, G. B. (2018). Extremely energetic rockfalls. *Journal of Geophysical Research: Earth Surface*, *123*(10), 2392–2421. https://doi.org/10.1029/2017JF004327

Dufresne, A., Bösmeier, A., & Prager, C. (2016). Sedimentology of rock avalanche deposits-Case study and review. *Earth-Science Reviews*, *16*, 234–259. https://doi.org/10.1016/j.earscirev.2016.10.002

Eberhardt, E., Stead, D., & Coggan, J. S. (2004). Numerical analysis of initiation and progressive failure in natural rock slopes—The 1991 Randa rockslide. *International Journal of Rock Mechanics and Mining Sciences*, *41*(1), 69–87. https://doi.org/10.1016/s1365-1609(03)00076-5

Gao, G., Meguid, M. A., Chouinard, L. E., & Zhan, W. (2021). Dynamic disintegration processes accompanying transport of an earthquake-induced landslide. *Landslides*, *18*(3), 909–933. https://doi.org/10.1007/s10346-020-01508-1

Haug, Ø. T., Rosenau, M., Leever, K., & Oncken, O. (2016). On the energy budgets of fragmenting rockfalls and rockslides: Insights from experiments. *Journal of Geophysical Research: Earth Surface*, *121*, 1310–1327. https://doi.org/10.1002/2014JF003406

Haug, Ø. T., Rosenau, M., Rudolf, M., Leever, K., & Oncken, O. (2021). Runout of rock avalanches limited by basal friction but controlled by fragmentation. *Earth Surface Dynamics*, *9*(3), 665–672. https://doi.org/10.5194/esurf-2020-76

Hsu, K. J. (1975). Catastrophic debris stream (Sturzstroms) generated by rockfalls. *Geological Society of America Bulletin*, *86*(1), 129–140. https://doi.org/10.1130/0016-7606(1975)86<129:cdssgb>2.0.co;2

Huang, R., Pei, X., Fan, X., Zhang, W., & Li, B. (2012). The characteristics and failure mechanism of the largest landslide triggered by the Wenchuan earthquake, May 12, 2008, China. *Landslides*, *9*(1), 131–142. https://doi.org/10.1007/s10346-011-0276-6

Kent, P. E. (1966). The transport mechanism in catastrophic rock falls. *The Journal of Geology*, *74*(1), 79–83. https://doi.org/10.1086/627142

Legros, F. (2002). The mobility of long runout landslides. *Engineering Geology*, *63*(3–4), 301–331. https://doi.org/10.1016/s0013-7952(01)00090-4

Li, K., Wang, Y. F., Cheng, Q. G., Lin, Q. W., Wu, Y., & Long, Y. M. (2022). Insight into granular flow dynamics relying on basal stress measurements: From experimental flume tests. *Journal of Geophysical Research: Solid Earth*, *127*(3), e2021JB022905. https://doi.org/10.1029/2021jb022905

Li, X. B., Lok, T. S., & Zhao, J. (2005). Dynamic characteristics of granite subjected to intermediate loading rate. *Rock Mechanics and Rock Engineering*, *38*(1), 21–39. https://doi.org/10.1007/s00603-004-0030-7

Lima, E. W. C. (2010). Granular Leidenfrost effect in vibrated beds with bumpy surfaces. *European Physical Journal E: Soft Matter*, *32*(4), 365–375. https://doi.org/10.1140/epje/i2010-10637-8

Lin, Q., Cheng, Q., Li, K., Xie, Y., & Wang, Y. (2020). Contributions of rock mass structure to the emplacement of fragmenting rockfalls and rockslides: Insights from laboratory experiments. *Journal of Geophysical Research: Solid Earth*, *125*(4), e2019JB019296. https://doi.org/10.1029/2019JB019296

Lin, Q., Wang, Y., Xie, Y., Cheng, Q., & Deng, K. (2022). Multiscale effects caused by the fracturing and fragmentation of rock blocks during rock mass movement: Implications for rock avalanche propagation. *Natural Hazards and Earth System Sciences*, *22*(2), 639–657. https://doi.org/10.5194/nhess-22-639-2022

Lin, Q.-W., Cheng, Q.-G., Xie, Y., Zhang, F.-S., Li, K., Wang, Y.-F., & Zhou, Y.-Y. (2020). Simulation of the fragmentation and propagation of jointed rock masses in rockslides: DEM modeling and physical experimental verification. *Landslides*, *18*(3), 993–1009. https://doi.org/10.1007/s10346-020-01542-z

Locat, P., Couture, R., Leroueil, S., Locat, J., & Jaboyedoff, M. (2006). Fragmentation energy in rock avalanches. *Canadian Geotechnical Journal*, *43*(8), 830–851. https://doi.org/10.1139/t06-045

McSaveney, M. J., & Davies, T. R. H. (2006). Rapid rock mass flow with dynamic fragmentation: Inferences from the morphology and internal structure of rockslides and rock avalanches. In S. G. Evans, G. S. Mugnozza, A. Strom, & R. L. Hermanns (Eds.), *Landslides from massive rock slope failure* (pp. 285–304). https://doi.org/10.1007/978-1-4020-4037-5_16

Melosh, H.-J. (1986). The physics of very large landslides. *Acta Mechanica*, *64*, 89–99. https://doi.org/10.1007/BF01180100

Mergili, M., Fischer, J. T., Krenn, J., & Pudasaini, S. P. (2017). r.avaflow v1, an advanced open-source computational framework for the propagation and interaction of two-phase mass flow. *Geoscientific Model Development*, *10*(2), 553–569. https://doi.org/10.5194/gmd-10-553-2017

Mergili, M., Jaboyedoff, M., Pullarello, J., & Pudasaini, S. P. (2020). Back calculation of the 2017 Piz Cengalo—Bondo landslide cascade with r.avaflow: What we can do and what we can learn. *Natural Hazards and Earth System Sciences*, *20*(2), 505–520. https://doi.org/10.5194/nhess-20-505-2020

Mergili, M., & Pudasaini, S. P. (2024). r.avaflow—The mass flow simulation tool [Software]. https://www.avaflow.org

Perinotto, H., Schneider, J. L., Bachelery, P., Le Bourdonnec, F. X., Famin, V., & Michon, L. (2015). The extreme mobility of debris avalanches: A new model of transport mechanism. *Journal of Geophysical Research: Solid Earth*, *120*(12), 8110–8119. https://doi.org/10.1002/2015JB011994

Pitman, E. B., & Le, L. (2005). A two-fluid model for avalanche and debris flows. *Philosophical Transactions of the Royal Society*, *A363*, 1573–1602. https://doi.org/10.1098/rsta.2005.1596

Pudasaini, S. P. (2012). A general two-phase debris flow model. *Journal of Geophysical Research*, *117*, F03010. https://doi.org/10.1029/2011JF002186

Pudasaini, S. P. (2024). A multi-phase thermo-mechanical model for rock-ice avalanche. *arXiv:2404.06130*.

Pudasaini, S. P., & Fischer, J.-T. (2020). A mechanical model for phase separation in debris flow. *International Journal of Multiphase Flow*, *129*, 103292. https://doi.org/10.1016/j.ijmultiphaseflow.2020.103292

Pudasaini, S. P., & Hutter, K. (2007). *Avalanche dynamics: Dynamics of rapid flows of dense granular avalanches*. Springer.

Pudasaini, S. P., & Krautblatter, M. (2014). A two-phase mechanical model for rock ice avalanches. *Journal of Geophysical Research: Earth Surface*, *119*(10), 2272–2290. https://doi.org/10.1002/2014jf003183

Pudasaini, S. P., & Krautblatter, M. (2021). The mechanics of landslide mobility with erosion. *Nature Communications*, *12*(1), 6793. https://doi.org/10.1038/s41467-021-26959-5

Pudasaini, S. P., & Mergili, M. (2019). A multi-phase mass flow model. *Journal of Geophysical Research: Earth Surface*, *124*(12), 2920–2942. https://doi.org/10.1029/2019jf005204

Pudasaini, S. P., & Mergili, M. (2024). Mechanically controlled landslide deformation. *Journal of Geophysical Research: Earth Surface*, *129*(5), e2023JF007466. https://doi.org/10.1029/2023JF007466

Pudasaini, S. P., Mergili, M., Lin, Q., & Wang, Y. (2024). r.avaflow package for fragmentation [Dataset]. *Zenodo*. https://doi.org/10.5281/zenodo.11243655

Pudasaini, S. P., & Miller, S. A. (2013). The hypermobility of huge landslides and avalanches. *Engineering Geology*, *157*, 124–132. https://doi.org/10.1016/j.enggeo.2013.01.012

Shreve, R. L. (1966). Sherman landslide, Alaska. *Science*, *154*(3757), 1639–1643. https://doi.org/10.1126/science.154.3757.1639

Shugar, D. H., Jacquemart, M., Shean, D., Bhushan, S., Upadhyay, K., Sattar, A., et al. (2021). A massive rock and ice avalanche caused the 2021 disaster at Chamoli, Indian Himalaya. *Science*, *373*(6552), 300–306. https://doi.org/10.1126/science.abh4455

Stead, D., Eberhardt, E., & Coggan, J. S. (2006). Developments in the characterization of complex rock slope deformation and failure using numerical modelling techniques. *Engineering Geology*, *83*(1–3), 217–235. https://doi.org/10.1016/j.enggeo.2005.06.033

Strom, A., & Abdrakhmatov, K. (2018). *Rockslides and rock avalanches of Central Asia: Distribution, morphology, and internal structure*. Elsevier.

Taberlet, N., Richard, P., Jenkins, J. T., & Delannay, R. (2007). Density inversion in rapid granular flows: The supported regime. *European Physical Journal E: Soft Matter*, *22*(1), 17–24. https://doi.org/10.1140/epje/e2007-00010-5

Turcotte, D. L. (1997). *Fractals and chaos in geology and geophysics*. Cambridge University Press.

Wang, Y. F., Cheng, Q. G., Shi, A. W., Yuan, Y. Q., Yin, B. M., & Qiu, Y. H. (2018). Sedimentary deformation structures in the Nyixoi Chongco rock avalanche: Implications on rock avalanche transport mechanisms. *Landslides*, *16*(3), 523–532. https://doi.org/10.1007/s10346-018-1117-7

Zhang, M., & McSaveney, M. J. (2017). Rock avalanche deposits store quantitative evidence on internal shear during runout. *Geophysical Research Letters*, *44*(17), 8814–8821. https://doi.org/10.1002/2017gl073774

Zhang, M., Wu, L. Z., Zhang, J. C., & Li, L. P. (2019). The 2009 Jiweishan rock avalanche, Wulong, China: Deposit characteristics and implications for its fragmentation. *Landslides*, *16*(5), 893–906. https://doi.org/10.1007/s10346-019-01142-6

Zhang, S.-L., Yin, Y.-P., Hu, X.-W., Wang, W.-P., & He, X.-R. (2023). Block-grain phase transition in rock avalanches: Insights from large-scale experiments. *Journal of Geophysical Research: Earth Surface*, *128*(11), e2023JF007204. https://doi.org/10.1029/2023JF007204

Zhang, Z. X., Kou, S. Q., Jiang, L. G., & Lindqvist, P. A. (2000). Effects of loading rate on rock fracture. *International Journal of Rock Mechanics and Mining Sciences*, *37*(5), 745–762. https://doi.org/10.1016/S1365-1609(00)00008-3